Title: miR-1 coordinately regulates lysosomal v-ATPase and biogenesis to affect muscle contractility upon proteotoxic challenge during ageing

[1, 8]Isabelle Schiffer, [1, 8]Birgit Gerisch, [1, 8]Kazuto Kawamura, [1]Raymond Laboy, [1, 3]Jennifer Hewitt, [1, 2]Martin S. Denzel, [4, 5, 6]Marcelo A. Mori, [3]Siva Vanapalli, [7]Yidong Shen, [1]Orsolya Symmons, [1, 2, 9]Adam Antebi

[1]Max Planck Institute for Biology of Ageing, Joseph Stelzmann Str. 9b, 50931, Cologne, Germany
[2]Cologne Excellence Cluster on Cellular Stress Responses in Aging-Associated Diseases (CECAD), University of Cologne, 50931, Cologne, Germany
[3]Department of Chemical Engineering, Texas Tech University, Lubbock, TX 79409, USA
[4]Laboratory of Aging Biology, Department of Biochemistry and Tissue Biology, University of Campinas (UNICAMP), Campinas, Brazil
[5]Experimental Medicine Research Cluster (EMRC), University of Campinas (UNICAMP), Campinas, Brazil
[6]Obesity and Comorbidities Research Center (OCRC), University of Campinas (UNICAMP), Campinas, Brazil
[7]State Key Laboratory of Cell Biology, Innovation Center for Cell Signaling Network, CAS Center for Excellence in Molecular Cell Science, Shanghai Institute of Biochemistry and Cell Biology, Chinese Academy of Sciences, University of Chinese Academy of Sciences
[8]co-first author
[9]corresponding author

Correspondence: aantebi@age.mpg.de

Abstract

Muscle function relies on the precise architecture of dynamic contractile elements, which must be fine-tuned to maintain motility throughout life. Muscle is also highly plastic, and remodelled in response to stress, growth, neural and metabolic inputs. The evolutionarily conserved muscle-enriched microRNA, miR-1, regulates distinct aspects of muscle biology during development, but whether it plays a role during ageing is unknown. Here we investigated the role of *C. elegans* miR-1 in muscle function in response to proteostatic stress during adulthood. *mir-1* deletion results in improved mid-life muscle motility, pharyngeal pumping, and organismal longevity under conditions of polyglutamine repeat proteotoxic challenge. We identified multiple vacuolar ATPase subunits as subject to miR-1 control, and the regulatory subunit *vha-13*/ATP6VIA as a direct target downregulated via its 3'UTR to mediate miR-1 physiology. miR-1 further regulates nuclear localization of lysosomal biogenesis factor HLH-30/TFEB and lysosomal acidification. In summary, our studies reveal that miR-1 coordinately regulates lysosomal v-ATPase and biogenesis to impact muscle function and health during ageing.

2

Introduction

Ageing is the major cause of progressive decline in all organ systems throughout the body. This is particularly evident in the musculature and often manifests as sarcopenia, the loss of muscle mass and strength. In fact, muscle frailty is a hallmark of tissue ageing seen in species as diverse as worms, flies, mice and humans (Herndon et al., 2002; Miller et al., 2008) (V. G. Martinez et al., 2007) (Demontis, Piccirillo, Goldberg, & Perrimon, 2013) (Cruz-Jentoft et al., 2010) (Nair, 2005). At the molecular level, frailty is often accompanied by a decline in muscle structure and function, as well as alterations in muscle proteostasis and metabolism. Nevertheless, muscle can respond positively to exercise and stress and rejuvenate even into older age, showing remarkable plasticity (Pollock et al., 2018) (Cartee, Hepple, Bamman, & Zierath, 2016) (Distefano & Goodpaster, 2018). A molecular study of muscle ageing and plasticity in a genetically tractable model could shed light on fundamental aspects of these processes.

microRNAs are small 22-26 nucleotide RNAs that bind with complementarity through their seed sequence to target mRNAs to downregulate gene expression (Gu & Kay, 2010). They can work as molecular switches or fine tune gene regulation, and typically have multiple targets, thereby coordinating cellular programs. Many microRNAs are expressed in a tissue-specific manner and regulate programs cell autonomously, and could therefore potentially serve as tissue-specific therapeutic targets (Guo et al., 2014) (Panwar, Omenn, & Guan, 2017). In addition, some microRNAs are found circulating in serum (Weber et al., 2010) (Chen et al., 2008), raising the possibility that they can act cell non-autonomously as well.

miR-1 homologs are muscle-enriched microRNAs that are highly conserved in evolution, and important for mammalian heart and muscle development (Zhao et al., 2007). Like in other animals, *Caenorhabditis elegans mir-1* is expressed in body wall ("skeletal") and pharyngeal ("cardiac") muscle (Simon et al., 2008). Deletion mutants are viable and exhibit modest changes in the behavior of the neuromuscular junction (Simon et al., 2008) and autophagy (Nehammer et al., 2019), but little else is known of its normative function. In this work, we examined the potential role of miR-1 in regulating muscle function and proteostasis. Surprisingly, we found that under polyQ35 proteotoxic challenge, *mir-1* mutation prevents aggregate formation, and increases organismal motility and pharyngeal contractility during ageing. Mechanistically, miR-1

3

78   regulates expression of several lysosomal v-ATPase subunits, and targets a crucial

79   regulatory component, *vha-13*/ATP6VIA, via its 3' UTR to impact proteotoxicity and

80   longevity. Further, miR-1 regulates lysosomal acidification and nuclear localization of

81   HLH-30/TFEB, a key regulator of lysosome biogenesis. These studies reveal an

82   unexpected role of miR-1 in coordinating lysosomal function and health during ageing.

83

84
85   **Results**

86   ***mir-1* mutation improves muscle motility upon polyQ challenge**

87   *mir-1* is a highly conserved microRNA expressed predominantly in muscle

88   tissues including pharyngeal muscle, body wall muscle, and sex muscles (Andachi &

89   Kohara, 2016; N. J. Martinez et al., 2008). To unravel molecular miR-1 function, we

90   first characterized the nature of several *mir-1* mutations. The reference alleles (*n4101,*

91   *n4102*) consist of large deletions of the region that could have confounding effects on

92   nearby loci. We therefore focused on *gk276*, a smaller 192 base pair deletion that

93   removes the *mir-1* coding region as well as the downstream non-coding region. We

94   also generated an independent *mir-1* allele, *dh1111,* by CRISPR genome engineering

95   (Figure 1A), which deletes a 52 base pair region within the *mir-1* locus. Both alleles

96   failed to express the mature miRNA as measured by Taqman qPCR (Supplemental

97   Figure 1A), and thus are *mir-1* null mutants.

98   To investigate *mir-1* function, we measured several physiological parameters.

99   We found that *mir-1* mutants *gk276* and *dh1111* developed normally, had normal brood

100   size, and near normal life span (Supplemental Figure 1B-D, Supplemental Table 1).

101   Additionally, motility on solid media, thrashing in liquid culture, and pharyngeal

102   pumping ability determined at day 8 and 14 of adulthood were similar to wild-type N2

103   controls (Supplemental Figure 1E-G, Supplemental Table 2). Since *mir-1* deletion

104   showed little obvious phenotype on its own, we reasoned that some physiological

105   differences might emerge under stress. However, we saw little distinction from wild-

106   type (WT) with moderate heat stress by growth at 25°C nor heat shock resistance at

107   35°C (Supplemental Figure 1D and H, Supplemental Table 1).
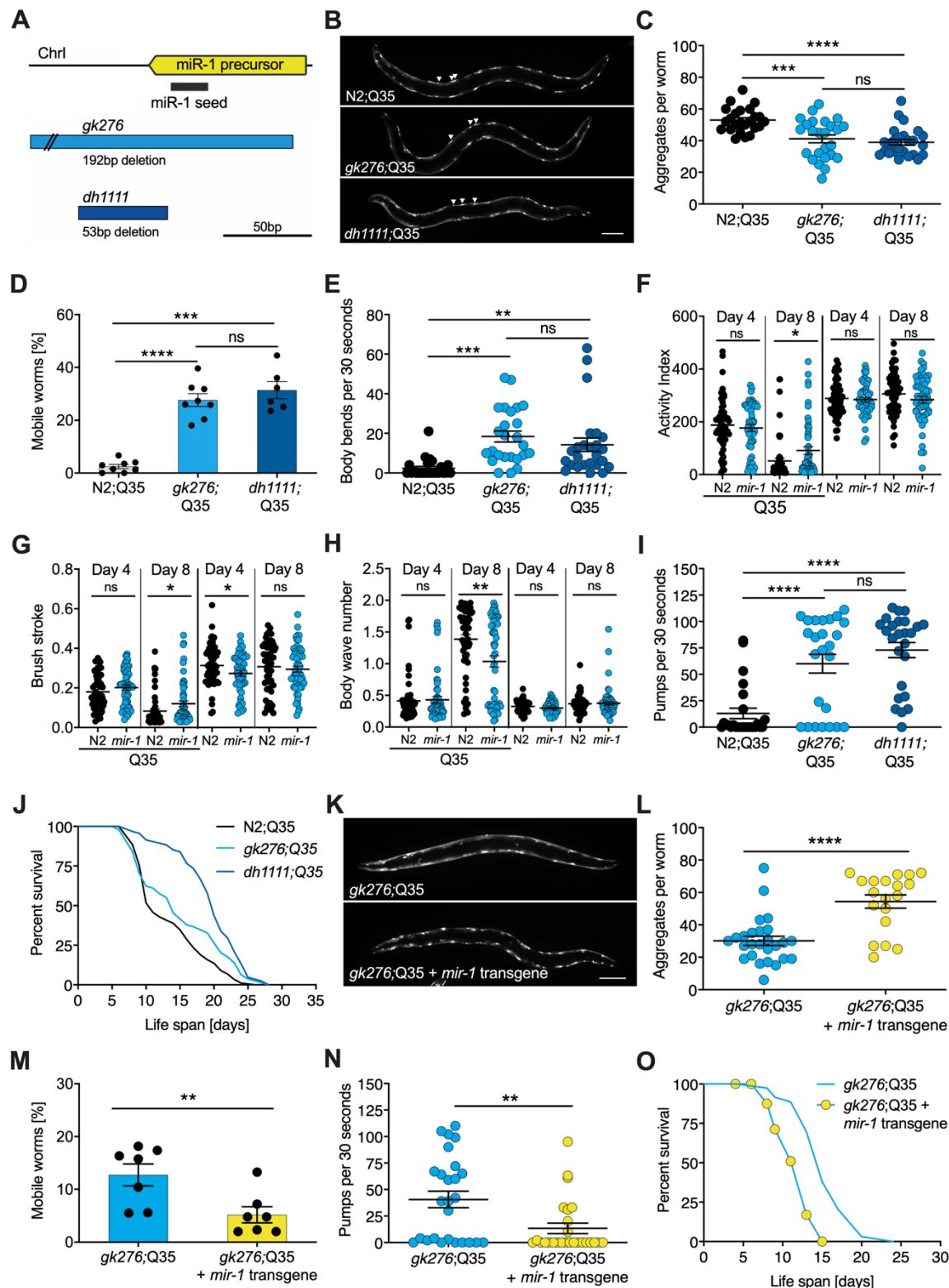

108

4

109

Figure 1. *mir-1* mutants exhibit improved motility upon polyQ challenge.

(A) Schematic showing the *mir-1* locus, deletion alleles *mir-1(gk276)* and *mir-1(dh1111)* (see Material and Methods).

(B) Representative images of wild-type N2 and *mir-1* mutant animals expressing *unc-54p::Q35::YFP* (Q35) showing loss of aggregates in the *mir-1* background on day 4 of adulthood. Arrowheads point to aggregates. Scale bar 100 μm. **(C)** Quantification of *Q35::YFP* aggregates in B using Zen software,

5

116   each dot represents one animal, mean ± SEM from one representative experiment, N=3, one way

117   ANOVA, Tukey´s multiple comparisons test, ***, p<0.001, ****, p<0.000, ns, not significant.

118   **(D)** Motility of indicated *mir-1* alleles and wild-type animals expressing *unc-54p::Q35::YFP*, measured

119   by the circle test, day 8 of adulthood. Percent worms that left the circle after 30 minutes was determined.

120   Each dot represents one experiment. Mean ± SEM of N=6 to 8. One way ANOVA, ***, p<0.001, ****,

121   p<0.0001, ns, not significant.

122   **(E)** Motility of *mir-1* alleles and wild-type animals expressing *unc-54p::Q35::YFP*, measured by the

123   thrashing assay. 25 worms per condition, each dot represents one animal, mean ± SEM from one

124   representative experiment, N=4, one way ANOVA, **, p<0.01 ***, p<0.001, ns, not significant.

125   CeleST analysis of activity index **(F)**, brush stroke **(G)** and body wave **(H)** comparing N2 and *mir-*

126   *1(gk276)* mutant animals with or without *unc-54p::Q35::YFP* at day 4 and day 8 of adulthood. Each dot

127   represents one animal. t-test, *, p<0.05 **, p<0.01, ns, not significant.

128   **(I)** Pharyngeal pumping rate measured on day 8 of adulthood in *mir-1* alleles and wild-type animals

129   expressing *unc-54p::Q35::YFP.* Each dot represents one animal, mean ± SEM from one representative

130   experiment, N=3, one way ANOVA, ****, p<0.0001, ns, not significant.

131   **(J)** Life span experiments of *mir-1* mutants and wild-type animals expressing *unc-54P::Q35::YFP.* One

132   experiment of N=3. t-test: N2;Q35 *vs. gk276*;Q35: p=0.03. N2;Q35 *vs. dh1111*;Q35: p<0.0001.

133   **(K)** Presence of an extrachromosomal *mir-1* transgene brings back aggregates in *mir-1(gk276)* mutants

134   at day 4 of adulthood, showing rescue by the transgene. Transgenic worms were compared to non-

135   transgenic segregants of the same strain. Scale bar 100 µm. **(L)** Quantification of *Q35::YFP* aggregates

136   (from **K**), each dot represents total aggregate number of one animal, mean ± SEM from one

137   representative experiment, N=3, t-test, ****, p<0.0001.

138   **(M)** Motility of *mir-1(gk276) unc-54p::Q35::YFP* animals in the presence or absence of the *mir-1*

139   transgene at day 8 of adulthood, measured by circle test. Each dot represents one experiment, mean ±

140   SEM of N=7. Total number of worms tested 646 (transgenic worms) and 469 (non-transgenic segregants

141   of the same strain), t-test, **, p<0.01.

142   **(N)** Pharyngeal pumping rate of *mir-1(gk276) unc-54p::Q35::YFP* animals in the presence or absence

143   of the *mir-1* transgene. Transgenic worms were compared to non-transgenic segregants of the same

144   strain. Each dot represents one animal, mean ± SEM from one representative experiment, N=7, t-test,

145   **, p<0.01.

146   (**O**) Life span experiments of *mir-1(gk276) unc-54p::Q35::YFP* animals in the presence or absence of

147   the *mir-1* transgene. Transgenic worms were compared to non-transgenic segregants of the same

148   strain. One representative experiment of N=5, t-test, p<0.0001.

149

150   We next tested the idea that *mir-1* mutants might differ in their response to

151   proteotoxic stress. To do so, we used a strain expressing polyglutamine-35 tracts fused

152   to yellow fluorescent protein (YFP) under the control of the muscle myosin specific

153   *unc-54* promoter (*unc-54p::Q35::YFP*), which has been used previously in models of

154   proteotoxicity and Huntington's disease (Morley, Brignull, Weyers, & Morimoto, 2002)

6

155   (Brignull, Morley, Garcia, & Morimoto, 2006). In these strains, initially soluble proteins
156   become sequestered into insoluble aggregates, visible as foci in the muscle of the
157   worm. Worms expressing the polyQ35 stretches showed progressive age-dependent
158   protein aggregation, which became clearly visible by day 4 of adulthood. Interestingly,
159   we observed that *mir-1* mutants displayed significantly less aggregates (avg. 38 and
160   36) compared to age-matched wild-type controls (avg. 53) at this time (Figure 1B and
161   C, Supplemental Table 2).

162   We further investigated the possible effect of proteotoxicity by measuring
163   organismal motility of Q35 strains using the circle test. This test measures how many
164   worms crawl out of a 1 cm circle within 30 minutes on day 8 of adulthood on agar
165   plates. Day 8 was chosen as a timepoint where paralysis becomes visible but animals
166   are still viable. We observed that about 30% of the *mir-1;*Q35 mutants left the circle
167   while only 2.5% of the control Q35 worms did so (Figure 1D, Supplemental Table 2).
168   We also measured motility by counting the thrashing rate in liquid culture on day 8 of
169   adulthood. Though the degree of paralysis was more variable, both *mir-1* mutants
170   *gk276* and *dh1111* were significantly more mobile (average 16, 15 body bends)
171   compared to age-matched wild-type controls (average 2 body bends, Figure 1E,
172   Supplemental Table 2).

173   To further characterize miR-1's impact on muscle function, we performed
174   CeleST analysis (Restif et al., 2014), a MATLAB based algorithm that extracts various
175   parameters of movement (wave initiation, travel speed, brush stroke, activity index)
176   and gait (wave number, asymmetry, curl, stretch) from video footage. Typically activity
177   measures decline with age, whereas gait abnormalities increase with age (Restif et al.,
178   2014). We scored animals focusing on day 4 and 8 of adulthood comparing *mir-1* and
179   WT, in the presence and absence of the Q35 array. In the absence of Q35, *mir-1*
180   mutants performed similar to WT (*e.g.*, body wave) or were slightly different (wave
181   initiation, travel speed, stretch) for some parameters (Supplemental Table 3). In the
182   presence of Q35, however, *mir-1* mutants did significantly better than WT for several
183   measures of activity (activity index, brush stroke, travel speed, wave initiation) and gait
184   (body wave) on day 8 (Figure 1F-H, Supplemental Figure 1I-M, Supplemental Table
185   3), consistent with the idea that *mir-1* mutation protects against proteotoxic stress
186   during mid-life.

187   *mir-1* is also highly expressed in the pharynx, a contractile tissue similar to
188   cardiac muscle. We observed that in the *mir-1*;Q35 background, pumping rate was
189   significantly increased (*gk276*, avg. 60; *dh1111*, avg. 78) compared to Q35 controls
190   (avg. 16) on day 8 of adulthood (Figure 1l, Supplemental Table 2). Furthermore, we
191   found that the life span of *mir-1(dh1111)*;Q35 strains was significantly extended (n=3,
192   mean 13 (WT) vs.19 (*dh1111*) days) compared to Q35 alone (Figure 1J, Supplemental
193   Table 1). A similar trend was seen with *gk276* in 2 of 3 experiments (Figure 1J,
194   Supplemental Table 1). These findings suggest that *mir-1* reduction can counter the
195   intrinsic and systemic detrimental effects of Q35 proteotoxic challenge.

196   Introducing a wild-type *mir-1* transgene into the *mir-1(gk276)* background
197   restored normal levels of *mir-1* expression (Supplemental Figure 1N) and largely
198   reversed *mir-1* phenotypes, showing increased Q35 aggregates, decreased motility,
199   pumping rate, and life span compared to non-transgenic controls (Figure 1K-O,
200   Supplemental Table 1 and 2). The similarity of behaviour among the different *mir-1*
201   alleles and the rescue of these phenotypes by the wild-type transgene demonstrate
202   that the *mir-1* mutation is causal for removing muscle aggregates and improving mid-
203   life motility.

204

v-ATPase subunits are downstream mediators of miR-1 induced motility
improvement

207   To identify downstream mediators of protein quality control improvement in
208   *mir-1* mutants, we used computational and proteomic approaches to find potential miR-
209   1 targets. For the computational approach, we used publicly available prediction tools
210   to identify genes harbouring miR-1 seed binding sites in their 3'UTR, namely
211   microRNA.org, TargetScanWorm, and PicTar (Betel, Wilson, Gabow, Marks, &
212   Sander, 2008) (Jan, Friedman, Ruby, & Bartel, 2011) (Lall et al., 2006). These
213   prediction tools use distinct algorithms that often yield different and extensive sets of
214   candidates (Figure 2A). Therefore, we limited ourselves mostly to candidates that were
215   predicted as targets by all three algorithms. This yielded 68 overlapping candidates
216   (Figure 2A), 50 of which had available RNAi clones (Supplementary Table 4).
217   Interestingly, network analysis of these 68 genes using STRING (string-db.org) (Snel,
218   Lehmann, Bork, & Huynen, 2000) revealed a tight cluster of predicted targets encoding
219   11/21 subunits of the vacuolar ATPase (Figure 2B, Supplemental Figure S2A). 5

220   additional vacuolar ATPase genes were identified by 2 of the 3 prediction algorithms
221   (Supplemental Figure 2A). In addition, two genes that code transcription factors
222   implicated in lysosome biogenesis, *daf-16*/FOXO and *hlh-30*/TFEB (Sardiello et al.,
223   2009; Settembre et al., 2011), also contained predicted miR-1 binding sites in their
224   3'UTRs.

225   Next, we carried out a functional screen of the selected candidates. We
226   reasoned that *mir-1* deletion likely results in an upregulation of these proteins, and that
227   RNAi knockdown of the relevant genes should therefore abrogate the improved motility
228   of *mir-1*;Q35 worms. Specifically, we scored motility using a rapid version of the circle
229   test, measuring the ability of *mir-1*;Q35 worms grown on candidate RNAis to migrate
230   out of a 1 cm diameter circle within 1 minute (Figure 2C). 12/20 *mir-1*;Q35 worms left
231   the circle when grown on luciferase control RNAi (*luci*). We considered genes as
232   potential *mir-1*;Q35 suppressors if less then 4 worms left the circle upon RNAi knock
233   down of the genes, and prioritized candidates when only 0 or 1 worms left. Among the
234   selected candidates vacuolar ATPase subunits *vha-1, vha-8, vha-9, vha-13,* and *vha-*
235   *14*, as well as muscle gene *zyx-1*, stood out as molecules suppressing *mir-1* motility
236   (Figure 2C and Supplemental Figure 2D).

237   As a second parallel approach to identify miR-1 regulatory targets in an
238   unbiased manner, we performed TMT shotgun proteomic analysis, comparing *mir-1*
239   mutants to WT worms on day 1 of adulthood. We identified approximately 1,500-2,000
240   proteins in the replicates (Figure 2D). Samples showed a high degree of correlation
241   (Supplemental Figure 2B) with minimal separation of WT and *mir-1* genotypes,
242   reflecting the subtle changes induced by *mir-1* mutation at the organismal level. For
243   further analysis we therefore selected the 50 top upregulated proteins with available
244   RNAi clones and tested them for their ability to suppress the motility phenotype using
245   the circle test (Supplemental Figure 2C and 2E, Supplemental Table 5), among them
246   *vha-10*, *vha-19* and *zyx-1*, which had previously been predicted to harbour *mir-1*
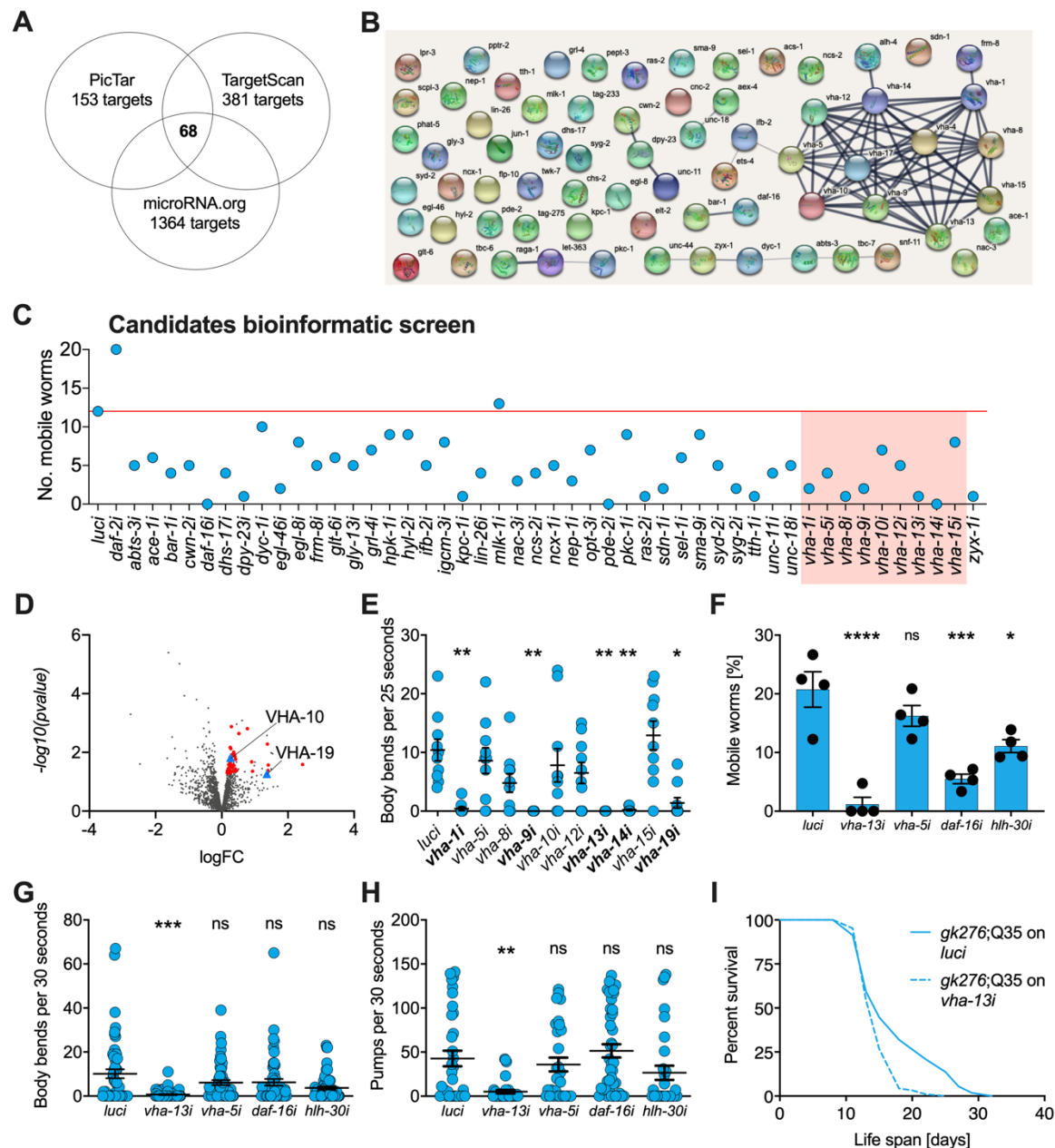247   binding sites.

248

9

Figure 2. v-ATPase subunits are downstream mediators of _mir-1_ induced motility improvement.

(A) Computational screen using _in silico_ prediction of miR-1 binding sites in target mRNAs using microRNA.org, TargetScan and PicTar identifies 68 shared candidates.

(B) STRING network analysis of predicted miR-1 targets reveals a cluster of vATPase subunits.

(C) Initial RNAi screen of computationally predicted candidates using the circle test on day 8 of adulthood reveals a number of candidates that reduced motility of _mir-1(gk276)_;Q35, 20 worms per RNAi (N=1). Red line, number of luciferase controls that left the circle. v-ATPases are highlighted in red.

(D) Volcano plot of proteomic analysis showing differentially regulated proteins in _mir-1_ vs. N2 animals. Red dots show upregulated proteins tested in circle assay, VHA-10 and VHA-19 indicated by blue triangles. N=6 (_mir-1_) and 4 (N2) biological replicates.

10

261 **(E)** Effect of v-ATPase subunit RNAi knockdown on *mir-1(gk276)*;Q35 motility as measured in the
262 thrashing assay. Animals are grown on the corresponding RNAi from L4 onwards. N=1. Mean ± SEM,
263 one way ANOVA, only significant values are labelled: *, $p < 0.05$, **, $p < 0.01$.
264 **(F)** and **(G)** Motility assay (circle test) and trashing assay on day 8 of *mir-1(gk276)*;Q35 worms upon
265 *vha-13, vha-5, daf-16 and hlh-30* RNAi knockdown. Control, luciferase RNAi (*luci*). Mean ± SEM of N=4,
266 one way ANOVA, *, $p < 0.05$, ***, $p < 0.001$, ****, $p < 0.0001$, ns, not significant.
267 **(H)** Pumping assay of *mir-1(gk276)*;Q35 worms upon *vha-13, vha-5, daf-16 and hlh-30* RNAi knockdown
268 on day 8 of adulthood. Control, luciferase RNAi (*luci*). N=3, mean ± SEM, one way ANOVA, **, $p < 0.01$,
269 ns, not significant.
270 **(I)** Life span of *mir-1*;Q35 and Q35 worms upon *vha-13* RNAi knockdown. One experiment of N=3, t-
271 test: $p < 0.01$.

272

273   Based on the prominent presence of vATPase genes among both the informatic
274 and the proteomic candidates, we systematically tested 10 of them in the thrashing
275 assay, confirming v-ATPase subunits *vha-1, vha-9, vha-13, vha-14* and *vha-19* as
276 likely mediators of *mir-1*;Q35 motility (Figure 2E). We further tested the impact of *vha-*
277 *5, vha-13* and transcription factors *daf-16/FOXO* and *hlh-30/TFEB* RNAi *on mir-1*;Q35
278 phenotypes in more detail, using the circle test, thrashing assay and pharyngeal
279 pumping as readout (Figure 2F-H), which again confirmed in particular the role of *vha-*
280 *13* in reducing *mir-1* motility. We also confirmed that the effect on motility was specific
281 to the *mir-1* background for *vha-5*, *vha-10*, *vha-13* and *hlh-30*, since RNAi of these
282 genes had no significant effect on motility in N2;Q35 worms (Supplemental Figure 2F).

283   In summary, knockdown of 5 of 10 tested v-ATPase subunits from both the
284 computational and proteomics screen, as well as 2 transcriptional mediators of
285 lysosome biogenesis, reduced or abolished *mir-1* motility improvement either by circle
286 test or thrashing, revealing these molecules to have congruent physiological effects.
287 Therefore, we focused most of our further efforts on examining v-ATPase regulation
288 by miR-1.

289

290 **miR-1 directly regulates VHA-13 protein levels in muscle tissue**
291   MicroRNAs regulate their targets by binding to the 3' UTR of client mRNAs,
292 thereby decreasing RNA stability and translation. If miR-1 regulates v-ATPase
293 subunits, then miR-1 loss would be predicted to de-repress v-ATPase mRNA and

11

294 protein levels. Because the onset of Q35 aggregation becomes visible by day 4 of
295 adulthood, we examined the mRNA expression of representative v-ATPase subunits
296 at this time. We found that the mRNA levels of *vha-5, vha-10, vha-13*, and *vha-19,* as
297 well as transcription factors *hlh-30*/TFEB and *daf-16*/FOXO were increased
298 approximately 2-fold in *mir-1* mutants compared to age-matched wild-type worms
299 (Figure 3A), consistent with the idea that these genes are miR-1 targets.

300   To investigate whether miR-1 also regulates candidates at protein level, we
301 endogenously tagged the v-ATPase subunits *vha-5, vha-10, vha-13* and *vha-19* by
302 CRISPR/Cas9 using an N-terminal 3xFlag-mNeonGreen-tag. Tagging *vha-19* and
303 *vha-10* caused lethality and were not pursued further. Tagged *vha-5* showed significant
304 upregulation in the pharynx in *mir-1* mutants compared to wild-type, but not in vulva
305 muscle (Supplementary Figure 3A and B, Supplemental Table 7). Furthermore, RNAi
306 knockdown only weakly suppressed *mir-1* motility (Figure 2E-G, Supplemental Table
307 S2). N-terminally tagged *vha-13(syb586),* however, was viable, showed expression
308 that was regulated, and harboured two potential *mir-1* binding sites in the 3' UTR
309 (Figure 3F, Supplemental Figure 3C). Moreover, *vha-13* RNAi (*vha-13i)* significantly
310 compromised the motility of *mir-1*;Q35 strains in the RNAi screens (Figure 2C), which
311 we further confirmed through thrashing assays and the circle test (Figure 2E-G). *vha-*
312 *13i* also significantly reduced pharyngeal pumping and life span in the *mir-1*;Q35
313 background compared to *luci* RNAi controls (Figures 2H and I, Supplemental Tables 1
314 and 2), yet had relatively minor effects on the motility of N2;Q35 itself (Supplemental
315 Figure 2F). We therefore focused on *vha-13* as a promising candidate to pursue in
316 depth for regulatory interactions with miR-1*.*

317   We first characterized the expression pattern of *3xFlag::mNeonGreen::vha-*
318 *13(syb586)* in more detail. The fusion protein was strongly expressed in the excretory
319 cell, canal, hypodermis, as well as gut (Figure 3B). In the hypodermis
320 *3xFlag::mNeonGreen::VHA-13* was localized in discrete foci (Figure 3B, Supplemental
321 Figure 3D). Notably, *3xFlag::mNeonGreen::VHA-13* also resided in miR-1 expressing
322 tissues of body wall muscle, sex muscles and pharynx, where it was more weakly
323 expressed. Within muscle cells, VHA-13 localized to dense bodies (analogous to
324 vertebrate Z disks) and intervening cytosol (Figure 3B, Supplemental Figure 3D).

325   Because *mir-1* is expressed in muscle tissues, we focused on quantifying the
326   expression of *vha-13* in these tissues. Strikingly, we observed that *VHA-13* levels were
327   upregulated in the pharyngeal isthmus of *mir-1* mutants (Figure 3C and D,
328   Supplemental Table 7), while conversely, overexpression of the *mir-1* transgene
329   decreased levels in this tissue relative to wild-type (Figure 3E, Supplemental Table 7).
330   To further investigate whether miR-1 directly regulates *vha-13*, we altered two
331   predicted miR-1 binding sites (BS) in the 3'UTR (Figure 3F). We first mutated miR-1
332   binding site 1 (*vha-13* BS1 *(syb504)*, at position 188-195 of *vha-13* 3'UTR), and then
333   additionally miR-1 binding site 2 (*vha-13* BS2 *(syb2180)*, at position 253-58 of *vha-13*
334   3'UTR) in the endogenously-tagged *vha-13(syb586)* strain. When only BS1 was
335   mutated, we still saw residual regulation of VHA-13 by miR-1 (Supplemental Figure
336   3E, Supplemental Table 7). Mutating both miR-1 binding sites (BS1,2: MUT2),
337   however, de-repressed VHA-13 levels in the isthmus in the WT background (Figure
338   3G). In double mutants containing both *mir-1* and *vha-13* BS1,2 mutations, no clear
339   regulation of *vha-13* expression was observed compared to the BS1,2 mutations alone
340   (Figure 3G), suggesting that miR-1 modulates pharyngeal *vha-13* expression through
341   both potential miR-1 BS sites.

342   We next sought to characterize *vha-13* regulation in the body wall muscle.
343   However, it was not possible to accurately measure expression in this tissue using the
344   *3xFlag::mNeonGreen::vha-13* strain due to the high expression levels in the adjacent
345   hypodermis and gut. We therefore generated transgenic worms expressing flag-
346   tagged *vha-13* containing its endogenous 3´UTR *(3xFlag::vha-13::vha-13* 3´UTR)
347   under control of the muscle-specific *myo-3* promoter. Consistent with results seen in
348   pharyngeal muscle, *vha-13* protein levels in the body wall muscle were also
349   upregulated in *mir-1* mutants compared to WT, as measured by Western blots (Figure
350   3H and I). Exchanging the *vha-13* 3´UTR with the *unc-54* 3'UTR lacking miR-1 binding
351   sites (*vha-13::unc-54 3´UTR*) blunted regulation by miR-1 (Figure 3H and I), indicating
352   that *vha-13* is repressed by miR-1 via its 3'UTR in both body wall and pharyngeal
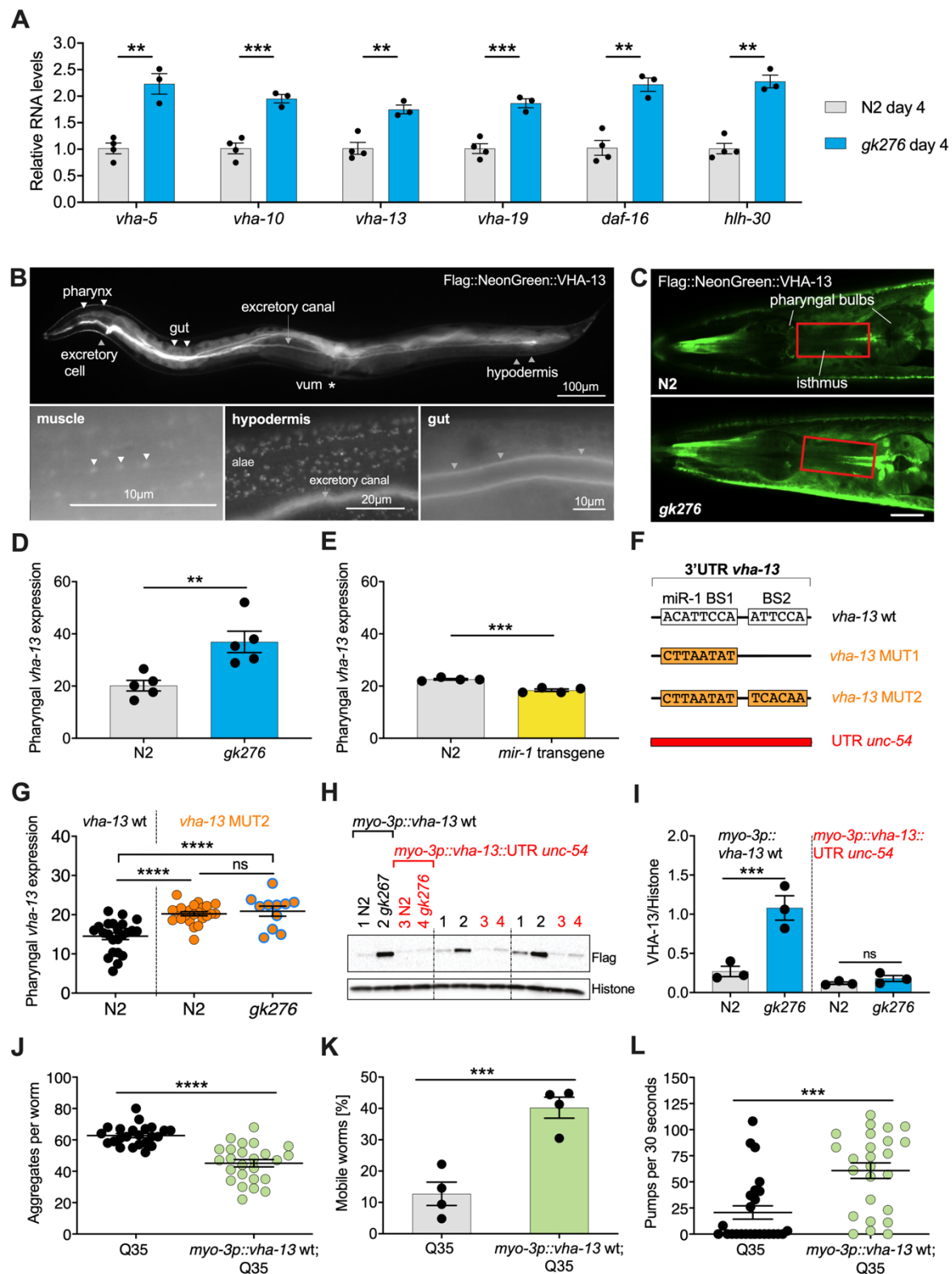353   muscle.

354

13

Figure 3. miR-1 directly regulates *vha-13* via its 3'UTR in muscle tissue.

(A) RT-qPCR of *vha-5, vha-10, vha-13* and *vha-19*, as well as *daf-16* and *hlh-30* mRNA levels in WT (N2) and *mir-1(gk276)* mutants on day 4 of adulthood. Mean ± SEM, N=3, one way ANOVA, **, p<0.01, ***, p<0.001.

(B) Expression pattern of endogenously tagged *3xFlag::mNeonGreen::vha-13* in pharynx, excretory cell and canal, gut, vulva muscle (vum), hypodermis, muscle (arrowhead indicates dense body).

14

(C) Confocal images of the head region in worms carrying endogenously tagged *3xFlag::mNeonGreen::vha-13* in late L4 *mir-1* and WT animals at 25°C. Red rectangle highlights the area of *vha-13* expression in the isthmus used for determination of mNeonGreen intensity. **(D)** Quantification of fluorescent intensity of *3xFlag::mNeonGreen::vha-13* expression in the isthmus of indicated genotypes (as shown in **(C)**) in late L4 larvae at 25°C. Mean ± SEM of N=5, t-test, **, p<0.01. **(E)** Quantification of fluorescent intensity of *3xFlag::mNeonGreen::vha-13* expression in the isthmus of N2; *mir-1* transgenic overexpression strain in late L4 larvae at 25°C. Transgenic worms (*mir-1* transgene) were compared to non-transgenic segregants (N2) of the same strain. Mean ± SEM of N=4, t-test, ***, p<0.001.

(F) Graphic showing the 3'UTR of endogenously tagged *3xFlag::mNeonGreen::vha-13. vha-13 wt: vha-13* wild-type 3´UTR. *vha-13* MUT1: one miR-1 binding site (BS) is mutated. *vha-13* MUT2: both miR-1 BSs are mutated. *unc-54*: the *vha-13* 3'UTR is substituted by *unc-54* 3'UTR. Nucleotide sequence of mutated miR-1 binding sites are shown below WT.

(G) Quantification of fluorescence intensity in the isthmus of L4 larvae with endogenously tagged *3xFlag::mNeonGreen::vha-13 vha-13 MUT2* 3'UTR in relation to *vha-13 wt* 3'UTR, in N2 and *mir-1(gk276)* mutant backgrounds at 25°C, using confocal imaging. Mean ± SEM of N=3, one representative experiment, one-way ANOVA, ****, p<0.0001, ns not significant.

(H) Western blot image of late L4 WT and *mir-1* mutants expressing transgenic flag-tagged *vha-13* in body wall muscle (*myo-3p*::*vha-13*) with either the *unc-54* 3´UTR (labelled in red), which lacks miR-1 BSs, or the wt *vha-13* 3´UTR which contains the two miR-1 BSs (labelled in black), immunoblotted with anti-Flag and anti-Histone H3 antibodies. Histone H3 loading control is shown below. Biological replicates (N=3) separated by dashed lines. **(I)** Quantification of Western blot shown in **(H)**, with flag-tag intensity normalized to histone H3 loading control, mean ± SEM of N=3, one-way ANOVA, ***, p<0.001, ns, not significant.

(J) Quantification of aggregates in Q35 worms expressing transgenic *vha-13* in the body wall muscle (*myo-3p*::*vha-13*;Q35) or non-transgenic segregants (Q35) of the same strain. 25 worms per genotype, mean ± SEM of one representative experiment, N=4, t-test, ***, p<0.001.

(K) Motility of Q35 worms expressing transgenic *vha-13* in the body wall muscle (*myo-3p*::*vha-13*;Q35) or non-transgenic segregants (Q35) of the same strain in circle test. Mean ± SEM. One experiment of N=2, t-test, ***, p<0.001.

(L) Pharyngeal pumping rate of *myo-3p*::*vha-13*;Q35 and Q35 non-transgenic segregants of the same strain. One representative experiment of N=4, mean ± SEM, t-test, ***, p<0.001.

Since *mir-1* mutation resulted in *vha-13* upregulation, we asked whether *vha-13* overexpression was sufficient to yield phenotypes similar to *mir-1* mutants. In accord with this idea, overexpressing *vha-13* in the muscle of Q35 worms significantly reduced aggregate number, improved motility, and enhanced pharyngeal pumping ability (Figure 3J-L, Supplemental Figure 3F, Supplemental Table 2). It also significantly increased the life span of Q35 animals compared to non-transgenic controls in 2/4 experiments (Supplemental Figure G, Supplemental Table 1). Altogether these data

15

402 suggest that miR-1 and VHA-13 work in the same regulatory pathway to influence
403 muscle physiology.
404

miR-1 regulates *hlh-30*/TFEB transcription factor

406 Our RT-PCR experiments indicated that miR-1 also regulates mRNA levels *hlh-*
407 *30/TFEB* and *daf-16*/FOXO transcription factors (Figure 3A). These factors modestly
408 affected motility in the circle test (Figure 2F), and we wondered if regulation extended
409 to the protein level. When we examined endogenously tagged *hlh-30*, we saw no
410 obvious regulation of protein expression levels when measured by fluorescence
411 intensity in the pharynx (Supplemental Figure 4A and B, Supplemental Table 7).
412 Surprisingly, however, we observed that nuclear localization of HLH-30::mNeonGreen
413 in the hypodermis of day 4 adults grown at 25°C was significantly increased in the *mir-*
414 *1* background (Figure 4A and 4B). This finding suggests that miR-1*,* either directly or
415 indirectly, regulates HLH-30 in distal tissues.

416

miR-1 affects lysosomal biogenesis

418 As the v-ATPase is an integral component of the lysosome, we asked wether
419 miR-1 generally affects lysosomal structure and function. To test this idea, we first used
420 a *lmp-1p::lmp-1::gfp* reporter strain. LMP-1 protein localizes to the membrane of
421 lysosomes and is a marker for lysosomal biogenesis (Hermann et al., 2005). LMP-1
422 protein levels were significantly increased in *mir-1* mutants compared to WT control,
423 as measured by Western blot analysis (Figure 4C and D). The v-ATPase hydrolyses
424 ATP to pump protons across the membrane, resulting in acidification of the lysosome
425 lumen (Beyenbach & Wieczorek, 2006). We therefore asked whether *mir-1* mutants
426 affect the number of acidified lysosomes. Using Lysotracker Red, a dye that targets
427 acidic membranous structures such as lysosomes (Chazotte, 2011), we observed an
428 increase in the number of acidified puncta in *mir-1* mutants at day 4 of adulthood
429 (Figure 4E and F). Due to technical limitations, lysotracker staining could only be
430 observed in the worm intestine. This result leaves open the question as to whether
431 lysosomes are also regulated in the muscle and whether *mir-1*, being expressed in
432 muscle tissue, might have a cell non-autonomous effect. Nonetheless, the overall
433 increase in lysosome biogenesis is consistent with the upregulation of lysosomal

434   components, such as the v-ATPase subunits, and a possible cause of miR-1-
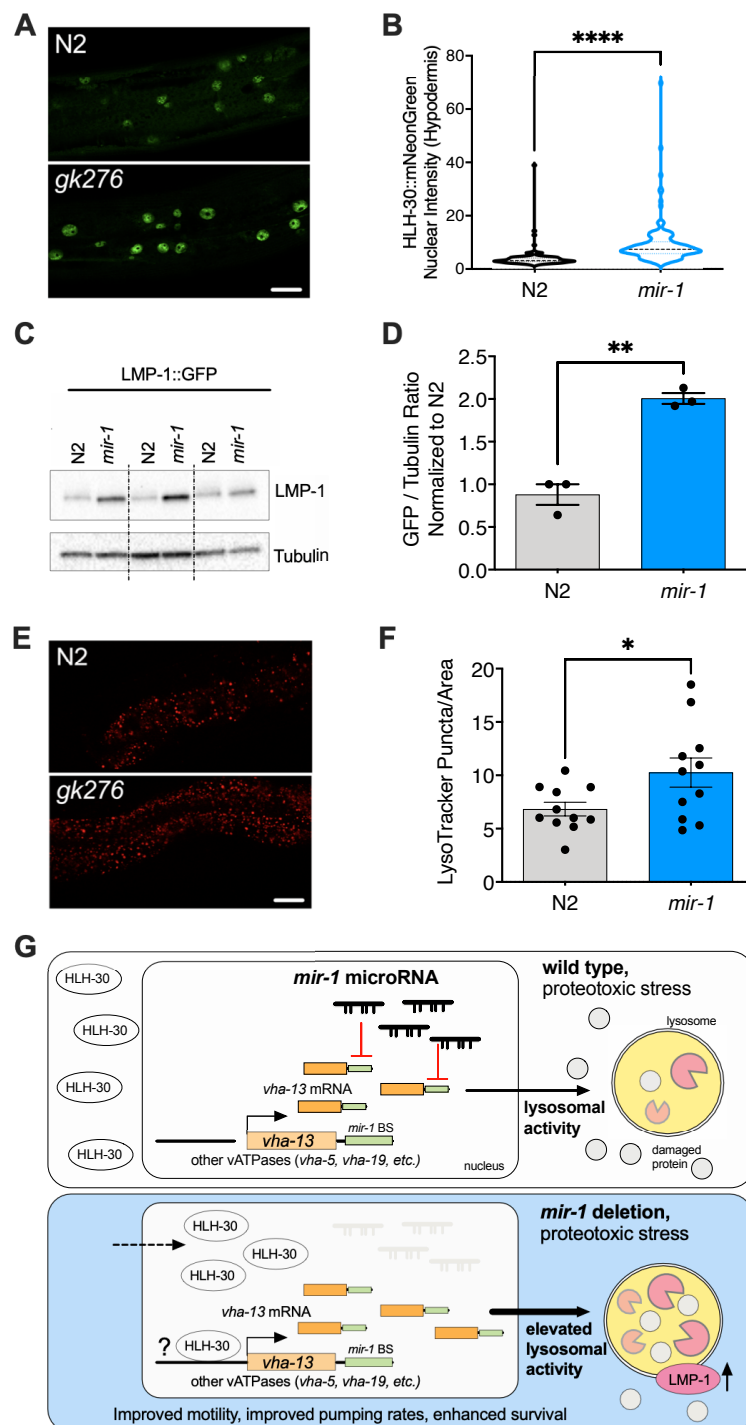
435   dependent regulation of proteostasis.

436

Figure 4. *mir-1* mutation enhances lysosomal biogenesis and acidification.

437

438   **(A)** Fluorescent image comparing HLH-30::mNeonGreen nuclear localization in the hypodermis of the

439   *mir-1(gk276)* and WT (N2) backgrounds. **(B)** Quantitation of nuclear localization in (A). Violin plot, mean

440   ± SEM of one representative experiment of N=3, t-test, ****, $p<0.0001$.

441   **(C)** Western blot of LMP-1::GFP in WT and *mir-1* mutants at the L4 stage, immunoblotted with anti-GFP

442   or anti-α-tubulin antibodies. Biological replicates (N=3) separated by dashed lines. **(D)** Quantification of

443   the Western blot in **(C),** normalized to α-tubulin loading control. N=3 BR, line and error bars indicate

444   mean ± SEM, t-test, **, p<0.01.

445   **(E)** Representative images of lysotracker staining in WT and *mir-1* mutants at day 4 of adulthood at

446   25°C. **(F)** Quantification of lysotracker images using a predefined squared area approximately spanning

447   the second to fourth gut cell. Quantification was performed using Image J. N=3 BR, line and error bars

448   indicate mean ± SEM of combined experiments, t-test, *, p<0.05.

449   **(G)** Working model. miR-1 normally limits proteoprotective pathways, downregulating the expression of

450   *vha-13,* other v-ATPases and factors by binding miR-1 binding site(s) in the 3'UTR (miR-1 BS) of the

451   corresponding mRNA (WT, proteotoxic stress). Loss of miR-1 under proteotoxic conditions results in

452   free *vha-13* mRNA, higher VAH-13 protein levels, and elevated lysosomal activity (LMP-1). Nuclear

453   localization of HLH-30/TFEB, a master regulator of lysosome biogenesis is also enhanced, collectively

454   resulting in improved mid-life muscle motility, pharyngeal pumping, and organismal longevity under

455   proteotoxic stress conditions.

456

457

458   **Discussion**

459   Striated muscle is one of the most highly ordered tissues in the body, with

460   molecular components organized in a lattice of contractile elements and attachments.

461   This molecular apparatus is exposed to high energy and force during contraction,

462   inflicting molecular damage requiring constant repair. Further, muscle is subject to

463   growth, metabolic, and stress signalling pathways as well as neural inputs that also

464   promote remodelling. Underlying muscle plasticity is the fine-tuned control of

465   proteostasis, including protein synthesis, folding, trafficking and turnover, which must

466   be precisely orchestrated to maintain muscle structure and function (Demontis et al.,

467   2013). A decline in these processes during aging leads to diminished muscle

468   performance and frailty, yet it remains elusive how various aspects of muscle

469   proteostasis are coordinated.

470   In this work, we discovered that the muscle enriched microRNA miR-1 plays an

471   important role in regulating muscle homeostasis via vacuolar ATPase function. Loss

472   of *mir-1* ameliorates age-related decline in motility induced by models of aggregate-

473   prone polyQ35. By inference, *mir-1* normally limits proteoprotective pathways.

474   Computational and proteomic screens identified v-ATPase subunits as highly enriched

475   targets of miR-1 regulation, suggestive of coordinate regulation, and whose

476   downregulation reduced proteoprotection. Expression studies confirmed that several

477   subunits (*e.g.*, *vha-5, vha-10, vha-13, vha-19*) showed miR-1 dependent regulation. In

478   particular, we demonstrated that *vha-13* expression is downregulated by miR-1 in

479   muscle tissues via two distinct binding sites in its 3'UTR. Moreover, VHA-13 links

480   miR-1 with muscle homeostasis, since *vha-13* downregulation abolished the improved

481   mid-life motility, pharyngeal pumping and life span of *mir-1*;Q35 strains, while *vha-13*

482   overexpression was sufficient to enhance these properties, similar to *mir-1* mutation.

483   In accord with our findings, immunoprecipitation and sequencing of microRNA

484   complexes revealed a number of v-ATPase subunit mRNAs, including *vha-13*, *vha-4,*

485   *vha-10,* and *vha-17* as physically associated with *C. elegans* miR-1 (Grosswendt et

486   al., 2014). Interestingly, mammalian homolog of VHA-13, ATP6V1A, as well as several

487   other v-ATPase subunits (Stark, Brennecke, Bushati, Russell, & Cohen, 2005),

488   harbour predicted miR-1 binding sites, suggesting that this regulatory module could be

489   conserved in evolution.

490   The v-ATPase is a multisubunit enzyme which acidifies the endolysosomal

491   lumen to control a plethora of cellular activities. Acidification regulates protein

492   trafficking, endocytic recycling, synaptic vesicle loading, and autophagy, as well as the

493   activity of multiple acid hydrolases and nutrient and ion transporters. Moreover, the v-

494   ATPase itself serves as a docking site for regulating mTOR and AMPK complexes and

495   affects metabolism (Settembre, Fraldi, Medina, & Ballabio, 2013; Zhang et al., 2014).

496   Our studies highlight the importance of v-ATPase activity to muscle performance. A

497   handful of studies ascribe a role for the v-ATPase in muscle. In mammalian

498   cardiomyocytes, lipid loading inhibits the v-ATPase, leading to a decline in contractile

499   function that could contribute to muscle deficits in diabetes (Wang et al., 2020). Lesions

500   in VMA21 that disrupt v-ATPase assembly have also been shown to cause myopathies

501   (Dowling, Moore, Kalimo, & Minassian, 2015). Conceivably the v-ATPase could play

502   an important role in protein turnover and remodeling of muscle structure but could also

503   impact muscle homeostasis through metabolic wiring or protein trafficking.

504   Surprisingly we also found that some *mir-1* phenotypes were not strictly limited

505   to muscle, since we observed a global increase in levels of lysosomal LMP-1::GFP in

506   Western blots, increased lysosomal acidification in the intestine, as well as enhanced

507   nuclear localization of HLH-30/TFEB in the hypodermis. Given that *mir-1* is muscle-

508   expressed, this observation could suggest cell non-autonomous regulation of

509   lysosomal biogenesis and associated activities by *mir-1*, acting either directly or

510   indirectly. Conceivably, miR-1 is secreted from muscle to affect physiology in other

511 tissues. In mammals miR-1 has been identified as a circulating microRNA found in

512 serum exosomes upon exercise stress or cardiac infarction, suggesting it could act

513 systemically (Cheng et al., 2019) (D'Souza et al., 2018). In this light, it is intriguing that

514 the v-ATPase itself is implicated in exosomal activity activity (Liegeois, Benedetto,

515 Garnier, Schwab, & Labouesse, 2006). Alternately, *mir-1* could act indirectly through

516 production of a myokine that affects distal tissues.

517   miR-1 has been implicated in regulating a number of targets and physiologic

518 processes. In mammals, miR-1 and its homolog miR-133 are essential to cardiac

519 development and function, where they have been shown to regulate Notch ligand

520 Dll-1, the GTPase dynamin 2 (DNM2), FZD7 (Frizzled-7), and FRS2 (fibroblast growth

521 factor receptor substrate 2) as targets (Ivey et al., 2008; Liu et al., 2011; Mitchelson &

522 Qin, 2015). Surprisingly knockout of mammalian *mir1/mir133* specifically in muscle has

523 little overt effect on muscle structure, but rather regulates the developmental transition

524 from glycolytic to oxidative metabolism via the MEF-2/Dlk1-Dio3 axis, affecting running

525 endurance (Wust et al., 2018). Similarly, *C. elegans* miR-1 regulates *mef-2*, in this case

526 affecting retrograde signalling at the neuromuscular junction (Simon et al., 2008). We

527 also observed that animals lacking *mir-1* have little overt change in muscle structure

528 or function alone, though we saw upregulation of a number of muscle proteins and

529 downregulation of mitochondrial proteins in our proteomic analysis. Indeed, most

530 microRNA knockouts do not lead to observable phenotypes in *C. elegans* (Miska et al.,

531 2007), suggesting that microRNAs often work redundantly or in response to stress to

532 fine tune gene expression.

533   Recently Pocock and colleagues reported that miR-1 downregulates the rab

534 GTPAse TBC-7/TBC1D15, thereby promoting autophagic flux in worms and human

535 cells (Nehammer et al., 2019). In *C. elegans* they observed that *mir-1(+)* ameliorates

536 polyQ40 proteotoxicity, seemingly contradicting our results. Other studies suggest that

537 mammalian *mir-1* can either promote or inhibit autophagy, dependent on context

538 (Ejlerskov, Rubinsztein, & Pocock, 2020; Hua, Zhu, & Wei, 2018; Xu, Cao, Zhang,

539 Zhang, & Yue, 2020). Whether miR-1 is proteoprotective or limits proteoprotection in

540 *C. elegans* could hinge on many factors. We used polyQ35, Pocock et al used

541 polyQ40; these species differ in the effect on aggregation and motility (Morley et al.,

542 2002). For motility assays, we assessed all animals that were alive, they excluded

543 paralyzed animals. We performed motility assays on day 8, they performed them

20

544   earlier in adulthood. Because microRNAs generally fine tune regulation, and often work

545   in feedback circuits, their impact on physiology can be subtle, and small differences in

546   culture conditions, genetic background, assay method, or metabolic state could give

547   rise to divergent outcomes.

548   Among the putative miR-1 targets that we identified in *C. elegans* are the pro-

549   longevity transcription factors DAF-16/FOXO and HLH-30/TFEB, which regulate

550   lysosome biogenesis, proteostasis, and metabolism, and act in insulin/IGF and mTOR

551   signalling pathways (Lin et al., 2018; O'Rourke & Ruvkun, 2013; Settembre et al.,

552   2011). *mir-1* mutation led to an upregulation of their mRNA during adulthood and

553   enhanced nuclear localization of HLH-30. Further RNAi knockdown of these factors

554   modestly diminished the motility improvement of *mir-1* mutants in the circle test,

555   consistent with roles in a miR-1 signalling pathway. Whether these transcription factors

556   are direct targets of miR-1 regulation remains to be seen. Notably*,* miR-1 predicted

557   targets also include pro-ageing components of mTOR signalling such as *let-363/*mTOR

558   and *raga-1/*RagA (targetscan.org), which also regulate the activity of these

559   transcription factors. Hence the balance or timing of pro- and anti-ageing factors could

560   also differentially influence the physiologic phenotype at a systemic level. Interestingly,

561   VHA-13/ATP6VIA subunit has been shown to regulate mTOR lysosomal recruitment

562   and activity (Chung et al., 2019) and mTOR signalling regulates the activity of TFEB

563   at the lysosomal surface (Settembre et al., 2013). Upregulation of v-ATPase activity is

564   also associated with the clearance of oxidized protein and rejuvenation of the *C.*

565   *elegans* germline (Bohnert & Kenyon, 2017). Thus, in the future it will be interesting to

566   further unravel the miR-1 molecular circuitry surrounding lysosomal function and

567   proteostasis, and see whether miR-1 similarly regulates v-ATPase function in humans.

568

569

Materials and Methods

C. elegans strains and culture

C. elegans strains were maintained at 20°C on nematode growth medium (NGM) plates seeded with a lawn of *E. coli* strain OP50, unless noted otherwise.

N2 Bristol (wild-type) CGC

AA2508, *mir-1(gk276)* I

AA4575, *mir-1(dh1111)* I

AM140, *rmIs132[unc-54p::Q35::YFP]* I

AA4403, *mir-1(gk276); rmIs132[unc-54p::Q35::YFP]* I

AA4577, *mir-1(dh1111) rmIs132[unc-54p::Q35::YFP*] I

AA3275, *N2; dhEx965[mir-1p::mir-1, myo-2p::mCherry]*

AA4810, *mir-1(gk276)* I*; rmIs132[unc-54p::Q35::YFP]; dhEx965[mir-1p::mir-1, myo-2p::mCherry]*

AA4865, N2; *dhEx1206[myo3p::flag::HA::mCherry::vha-13cDNA::unc-54* 3'UTR*, myo-2p::GFP]*

AA4866*, mir-1(gk276)* I*; dhEx1206[myo-3p::flag::HA::mCherry::vha-13cDNA::unc-54* 3'UTR*, myo-2p::GFP]*

AA5067, N2; dh*Ex1207[myo-3p::flag::HA::mCherry::vha-13cDNA::vha-13 3'UTR, myo-2p::GFP]*

AA5068, *mir-1(gk276)* I*; dhEx1207[myo-3p::flag::HA::mCherry::vha-13cDNA::vha-13 3'UTR, myo-2p::GFP]*

PHX586, *vha-13(syb586[3xFlag::mNeonGreen::vha-13])* V

AA4813, *mir-1(gk276)* I; *vha-13(syb586[3xFlag::mNeonGreen::vha-13])* V

AA4850, *vha-13(syb586[3xFlag::mNeonGreen::vha-13])* V; *dhEx965[mir-1p::mir-1, myo-2p::mCherry]*

PHX587, *vha-13(syb587,syb504[3xFlag::mNeonGreen::vha-13* miR-1 BS1 mutated*])* V. Also named in the text *vha-13* MUT1.

AA4184, *mir-1(gk276)* I; *vha-13(syb587,syb504[3xFlag::mNeonGreen::vha-13* miR-1 BS1 mutated*])* V

PHX2180, *vha-13(syb2180,syb587,syb504[3xFlag::mNeonGreen::vha-13* miR-1 BS1,2 mutated*])* V. Also named in the text *vha-13* MUT2.

AA5123, *mir-1(gk276)* I; *vha-13(syb2180,syb587,syb504[3xFlag::mNeonGreen::vha-13* miR-1 BS,2 mutated*])* V

604   PHX1093, *vha-5(syb1093[3xFlag::mNeonGreen::vha-5])* IV

605   AA5069, *mir-1(gk276)* I; *vha-5(syb1093[3xFlag::mNeonGreen::vha-5])* IV

606   PHX809, *hlh-30(syb809[hlh-30::mNeonGreen])* IV

607   AA5195, *mir-1(gk276)* I; *hlh-30(syb809[hlh-30::mNeonGreen])* IV

608

Molecular cloning

610   All restriction digest reactions were performed with enzymes provided by NEB
according to the user's manual. T4 DNA Ligase (NEB) was used for ligation reactions.
Chemically competent DH5α *Escherichia coli* (LifeTechnologies) was used for
transformation following the manufacturer's instructions. QIAprep Miniprep or Midiprep
Kits (Qiagen) were used for plasmid purification. Cloning was verified by PCR followed
by gel electrophoresis and sequencing.

616   To make the rescuing *mir-1* transgene, primer pair "celmir1fwd2/rvs2" (Table
S8) was used to insert the *mir-1* coding region into vector L3781 downstream of *gfp*.
The *mir-1* promoter was then cloned 5' to *gfp* using the primer pair "m1p fwd/rvs"(Table
S8). To make muscle expressed *vha-13* constructs, the *vha-13* cDNA was amplified
with Kpn1 overhangs using primers vha-13 fwd/rvs (Table S8) and cloned into vector
pDESTR4-R3 to give *myo3p::flag::HA::mCherry::vha-13cDNA::unc-54* 3'UTR. The
unc-54 3'UTR was excised with Not1/BglI and replaced with the *vha-13* 3'UTR using
primers vha-13U fwd/rvs (Table S8) to generate *myo3p::flag::HA::mCherry::vha-13cDNA::vha-13 3'UTR.*

625

Generation of transgenic worm strains

627   Transgenic worms containing extrachromosomal arrays were generated by
microinjection. To generate the ***myo3p::flag::HA::mCherry::vha-13cDNA::unc-54
3'UTR*** strain, a mix of *myo3p::flag::HA::mCherry::vha-13cDNA::unc-54* 3'UTR DNA
(40ng/ μl), *myo-2p::gfp* co-transformation marker (5 ng/ μl plasmid pPD122.11) and
fill DNA (TOPO empty vector, 55 ng/ μl) was injected into young N2 adults using an
Axio Imager Z1 microscope (Zeiss) with a manual micromanipulator (Narishige)
connected to a microinjector (FemtoJet 4x, Eppendorf). We obtained the strain
AA4865: N2*; dhEx1206[myo3p::flag::HA::mCherry::vha-13cDNA::unc-54 3'UTR, myo-2p::gfp]*, which was then used to cross the transgene into other genetic backgrounds.

23

636   A similar strategy was used to create AA5067, N2;

637   dh*Ex1207[myo3p::flag::HA::mCherry::vha-13cDNA::vha-13 3'UTR, myo-2p::GFP]*.

638

639   The ***mir-1 transgene*** strain was generated by injection mix containing *mir-*

640   *1p::mir-1* plasmid, *myo-2p::mCherry* co-transformation marker (5 ng/ µl plasmid

641   pPD122.11) and fill DNA (L3781 empty vector). The resultant strain AA3275 (*N2;*

642   *dhEx965[mir-1p::mir-1, myo-2p::mCherry]*) was then used to cross the *dhEx965*

643   transgene to *mir-1(gk276); rmIs132[p(unc-54) Q35::YFP]* to give *mir-1(gk276);*

644   *rmIs132[p(unc-54) Q35::YFP]; dhEx965[mir-1p::mir-1, myo-2p::mCherry]*, AA4810.

645   For transgenic worm strains, non-transgenic worms of the same strain were used as

646   controls.

647   The ***mir-1 deletion allele dh1111*** was generated using CRISPR/Cas9

648   mutagenesis. We designed CRISPR guides using the EnGen sgRNA Designer

649   (https://sgrna.neb.com/#!/sgrna), synthesized guides with the Engen sgRNA synthesis

650   kit and analysed them by gel electrophoresis and tape station. We injected worms with

651   an injection mix containing Cas9 EnGen (NEB), 4 sgRNAs against *mir-1*

652   (AAGAAGTATGTAGAACGGGG, GTAAAGAAGTATGTAGAACG,

653   TATAGAGTAGAATTGAATCT, ATATAGAGTAGAATTGAATC), one sgRNA against

654   *dpy-10* (CGCTACCATAGGCACCACG), KCl, Hepes pH 7.4 and water. Prior to

655   injection we incubated the mixture for 10 minutes at 37°C to allow activation of Cas9.

656   Following injection, we singled out worms with Dpy phenotype in the F1 generation

657   and genotyped them for *mir-1* deletion using *mir-1* genotyping primers (Supplemental

658   Table 8). We sequenced the PCR products of candidate worms with Sanger

659   sequencing and verified that the deletions resulted in loss of *mir-1* expression using

660   Taqman-based quantification of mature miRNA levels.

661   **Endogenous fluorescently tagged strains** were generated by tagging *vha-5*

662   or *vha-13* with 3xFLAG-mNeonGreen tag at the N-terminus using CRISPR–Cas9

663   (SunyBiotech). The *vha-13* 3'UTR mutants BS1 and BS2 were generated using

664   CRISPR–Cas9, by further mutating one or both putative miR-1 binding sites in the

665   3'UTR of the endogenous FLAG-mNeonGreen-tagged *vha-13 gene* (SunyBiotech).

666   PHX809 *hlh-30::mNeonGreen* endogenously tagged *hlh-30* was generated by placing

667   *mNeonGreen* at the C-terminus using CRISPR–Cas9 (SunyBiotech).

668

Determination of progeny number

Single worms were maintained on an NGM agar plate and transferred every day until the reproductive period was complete. The number of F1 progeny per individual worm was counted at the L4 or young adult stage. Experiments were repeated at least three times.

Quantitation of polyQ aggregates

Whole-worm images of day 4 adults were taken with an Axiocam 506 mono (Zeiss) camera using the 5x objective of a Zeiss Axio Imager Z1 microscope (20ms exposure). Q35 aggregate numbers were evaluated from photos at 163% magnification. Genotypes of the samples were blinded during the counting. Aggregates were defined as discrete structures or puncta above background.

Motility, thrashing and pumping behaviour

To analyse worm motility by the circle test, 20 to 25 worms were placed in the centre of a 6 cm agar plate with bacteria, marked with 1 cm circle on the bottom. After a defined time period (1 or 30 minutes) the number of worms that left the circle were counted. To determine thrashing rate, individual worms were transferred to M9 buffer and the number of body bends in a 20 to 30 second interval was scored. Pharyngeal pumping rates were measured by counting grinder contraction in the terminal bulb over 20 to 30 seconds. Genotypes were blinded during all experiments.

CeleST Assay

The *C. elegans* Swim Test (CeleST) assay was used to assess animal motility while swimming; assays were conducted as described previously (Ibanez-Ventoso, Herrera, Chen, Motto, & Driscoll, 2016; Restif et al., 2014). Four or five animals were picked and placed into the swimming arena, which was a 50 µl aliquot of M9 Buffer inside a 10 mm pre-printed ring on the surface of a glass microscope slide (Thermo Fisher Scientific). Images of the animals within the swim arena were acquired with a LEICA MDG41 microscope at 1x magnification with a Leica DFC3000G camera. Image sequences of 30 seconds in duration were captured at a rate of ~16 frames per second. The established CeleST software was used to process the image sequences and extract 8 measures that are descriptive of *C. elegans* swim motility. As not all images in a sequence are always successfully processed by the CeleST software, animals for which fewer than 80% of frames were valid were excluded from the analysis. For each

703 measure, single measurements that did not fit within the range of normally observed

704 values were deemed outliers and also excluded from the analysis. Unpaired Student's

705 t-test was used to test for statistical significance between two strains at adult day 4 and

706 day 8.

707

Life span and heat stress experiments

709 Life span experiments were performed as described (Gerisch et al., 2007). Day

710 0 corresponds to the L4 stage. Life spans were determined by scoring a population of

711 100 to 120 worms per genotype every day or every other day. Worms that exploded,

712 had internal hatch or left the plate were censored. Heat stress experiments were

713 performed at 35°C (Gerisch et al., 2007). Day 1 adult worms were transferred onto pre-

714 heated (35°C) plates 6 cm plates seeded with OP50. Worms were kept at 35°C and

715 scored every hour for live versus dead. Experiments were repeated at least three

716 times. Data were analysed with Microsoft Excel 16.12 and GraphPad Prism 7

717 Software. *P*-values were calculated using the Log-rank (Mantel-Cox) test to compare

718 two independent populations.

719

RNAi Treatment

721 Worms were grown from L4 onwards unless mentioned otherwise on *E. coli*

722 HT115 (DE3) bacteria expressing dsRNA of the target gene under the control of an

723 IPTG-inducible promotor. RNAi colonies were grown overnight at 37°C in Luria Broth

724 with 50 µg/ml Ampicillin and 10 µg/ml tetracycline. The cultures were spun down at

725 4,000 rpm at 4°C for 10 minutes. 500 µl of one-fold concentrated culture was seeded

726 onto NGM plates containing 1 M isopropyl β-D-1-thiogalactopyranoside (IPTG) to

727 induce dsRNA expression. RNAi clones were selected from the Ahringer or Vidal

728 library (Kamath & Ahringer, 2003; Rual et al., 2004). Clone identity was confirmed by

729 sequencing. Bacteria containing luciferase were used as control.

730

RNAi screen for *mir-1* suppressors

732 *mir-1(gk276)* Q35 worms were grown from L4 on RNAi of the candidates

733 identified in the bioinformatic or proteomic screen. Worms were maintained in the

734 presence of FUDR till day 8 of adulthood. The circle test was performed as described

735 above. The number of worms that left the circle was determined after 1 minute.

736 Selected candidates identified in the circle test were examined in the body bending

737 assay (see above). The effect of selected candidate RNAi clones was additionally

738 tested on polyQ35 in the wild-type background as counter screen. For this experiment

739 worms were grown till day 5 of adulthood. Motility assays were performed on day 5 of

740 adulthood because Q35 wild-type worms were less motile than the *mir-1(gk276)* Q35

741 and were largely paralyzed by day 8.

742

743 **RNA extraction and real-time qPCR analysis**

744 Worm populations (ca. 500 animals) were harvested on day 4 of adulthood and

745 washed twice in cold M9. Worm pellets were taken up in 700 µl QIAzol reagent

746 (Qiagen) and snap frozen in liquid nitrogen. Samples were subjected to 4 freeze/thaw

747 cycles and homogenized with 1.0 mm zirconia/silica beads (Fisher Scientific) in a

748 Tissue Lyser LT (Qiagen) for 15 min at full speed. After homogenization, 600µl

749 supernatant was transferred to fresh tubes and 120 µl chloroform were added to each

750 tube. Components were mixed by vortexing and incubated for 2 min at room

751 temperature. After 15 min centrifugation at 12,000 *g* 4°C, the aqueous phase was

752 collected for total RNA extraction using the RNeasy or miRNeasy Mini Kit (Qiagen)

753 according to manufacturer's instructions. RNA quantity and quality were determined

754 on a NanoDrop 2000c (PeqLab) and cDNA was prepared using the iScript cDNA

755 Synthesis Kit (BioRad). To quantify RNA expression, we used the Power SYBR Green

756 Master Mix (Applied Biosystems) on a ViiA 7 Real-Time PCR system (Applied

757 Biosystems). Four technical replicates were pipetted on a 384-well plate using the

758 JANUS automated workstation (PerkinElmer). Expression of target RNA was

759 calculated from comparative CT values, normalized to *ama-1* or *cdc-42* as internal

760 controls using the corresponding ViiA7 software. All unpublished primers were

761 validated by determination of their standard curves and melting properties. For

762 quantification of *mir-1* we used Taqman probes from LifeTechnologies/ThermoFisher

763 Scientific (Assay ID 000385) and normalized to expression of U18 as measured by

764 Taqman probes from LifeTechnologies/ThermoFisher Scientific (Assay ID 001764).

765 We used N=4 independent biological replicates, and four technical replicates for every

766 biological sample (for primers, refer to Supplementary Table 8).

767

768 **Western blot analysis**

769 For Western blot analysis synchronized young adult or gravid day 1 adult worms

770 were picked into Eppendorf tubes containing M9, snap frozen in liquid nitrogen and

771 lysed in 4x SDS sample buffer (Thermo Fisher) containing 50 mM DTT. After boiling

772 and sonication, equal volumes were subjected to reducing SDS-PAGE and transferred

773 to nitrocellulose membranes. The membranes were then blocked for two hours at room

774 temperature in 5% milk in Tris-buffered Saline and Tween20 (TBST) and probed with

775 the primary antibodies in TBST with 5% milk overnight at 4 °C. Specific secondary

776 antibodies (mouse or rabbit) were used at a concentration of 1:5000 in TBST with 5%

777 milk at room temperature for 2 hours. The membranes were developed with Western

778 Lightening Plus- Enhanced Chemiluminescence Substrate (PerkinElmer). Bands were

779 detected on a ChemiDoc MP Imaging System (BioRad) and the intensity quantified

780 using the corresponding Image Lab software (BioRad). The following antibodies were

781 used: anti-GFP (JL-8 Living Colors, mouse monoclonal), anti-Histone H3 (ab1791

782 Abcam, rabbit polyclonal), anti-α-Tubulin (T6199 Sigma, mouse monoclonal), anti-

783 FLAG (F1804 Sigma, mouse monoclonal), anti-mouse IgG (G-21040 Invitrogen, goat

784 polyclonal coupled with horseradish peroxidase), anti-rabbit IgG (G-21234 Invitrogen,

785 goat polyclonal coupled with horseradish peroxidase).

786

787 **Proteomic analysis**

788 For **sample collection and preparation**, day 1 N2 and *mir-1(gk276)* worms

789 were synchronized by egg laying, and $n \geq 5000$ worms per genotype were collected in

790 M9. Samples were washed three times in M9 and directly frozen in liquid nitrogen and

791 stored at –80 °C. 5 independent biological replicates of each genotype were collected

792 for further analyses. For **protein extraction** samples were thawed and boiled in lysis

793 buffer (100 mM Tris-HCl, 6 M guanidinium chloride, 10 mM Tris(2-

794 carboxyethyl)phosphine hydrochloride, 40 mM 2-Chloroacetamide) for 10 min, lysed

795 at high performance with a Bioruptor Plus sonicator (Diagenode) using 10 cycles of 30

796 s sonication intervals. The samples were then boiled again, centrifuged at 20000*g* for

797 20 min, and diluted 1:10 in 20 mM Tris pH 8.3 / 10% acetonitrile (ACN). Protein

798 concentration was measured using BCA Protein Assays (Thermo Fisher). Samples

799 were then digested overnight with rLys-C (Promega), the peptides were cleaned on a

800 Supelco Visiprep SPE Vacuum Manifold (Sigma) using OASIS HLB Extraction

801 cartridges (Waters). The columns were conditioned twice with Methanol, equilibrated

802 twice with 0.1% formic acid, loaded with the sample, washed three times with 0.1%

803 formic acid and the peptides eluted with 60% ACN / 0.1% formic acid. The samples

804 were dried at 30°C for roughly 4 h in a Concentrator (Eppendorf) set for volatile

805 aqueous substances. The dried peptides were taken up in 0.1% formic acid and the

806 samples were analysed by the Max Planck Proteomic Core facility. **Mass**
807 **spectrometry** data acquisition, computational proteomic analysis and differential
808 expression analysis were performed as described (Tharyan et al., 2020). Upon
809 inspection of the numbers of quantified proteins and the raw proteomic data, two
810 replicates of N2 were excluded from further analysis.

811

Microscopy and expression analysis

813 For confocal microscopy *vha-13*, *vha-5 and hlh-30* endogenously tagged with
814 mNeonGreen were synchronized via egg and maintained at 25°C to induce mild stress.
815 *hlh-30* worms were imaged as day 4 adults, while *vha-13* and *vha-5* worms as L4s,
816 because of high mNeonGreen background expression at day 4 adulthood. Worms
817 were anaesthetized with 40 μM sodium azide, mounted on slide with 2% agar pad and
818 imaged with a Leica TCS SP8 microscope equipped with HC PL APO CS2 63X/1.40
819 Oil and white light laser. Images were analysed using photoshop or Fiji software. To
820 quantitate acidic lysosomes, worms grown at 25°C were incubated 48 hours prior to
821 imaging with 2 μM LysoTracker Red DND-99 (Life Technologies). Worms were imaged
822 as day 4 adults as described above. Number of puncta in a predefined squared area
823 in the intestine (approximately spanning the second to fourth gut cell) were counted.

824

Statistical Analysis

826 The statistical tests performed in this study are indicated in figure legends and
827 in the method detail section. Data are represented as mean ± SEM or as individual
828 data points, as stated in the figure legends. Number of replicates and animals for each
829 experiment are enclosed in their respective figure legends.

830

Data and Software Availability

832 Accession Code: The mass spectrometry proteomics data have been
833 deposited to the ProteomeXchange Consortium via the PRIDE partner repository
834 (Perez-Riverol et al., 2019) with the dataset identifier PXD023544.

835

References

Andachi, Y., & Kohara, Y. (2016). A whole-mount in situ hybridization method for microRNA detection in Caenorhabditis elegans. *RNA, 22*(7), 1099-1106. doi:10.1261/rna.054239.115

Betel, D., Wilson, M., Gabow, A., Marks, D. S., & Sander, C. (2008). The microRNA.org resource: targets and expression. *Nucleic Acids Res, 36*(Database issue), D149-153. doi:10.1093/nar/gkm995

Beyenbach, K. W., & Wieczorek, H. (2006). The V-type H+ ATPase: molecular structure and function, physiological roles and regulation. *J Exp Biol, 209*(Pt 4), 577-589. doi:10.1242/jeb.02014

Bohnert, K. A., & Kenyon, C. (2017). A lysosomal switch triggers proteostasis renewal in the immortal C. elegans germ lineage. *Nature, 551*(7682), 629-633. doi:10.1038/nature24620

Brignull, H. R., Morley, J. F., Garcia, S. M., & Morimoto, R. I. (2006). Modeling polyglutamine pathogenesis in C. elegans. *Methods Enzymol, 412*, 256-282. doi:10.1016/S0076-6879(06)12016-9

Cartee, G. D., Hepple, R. T., Bamman, M. M., & Zierath, J. R. (2016). Exercise Promotes Healthy Aging of Skeletal Muscle. *Cell Metab, 23*(6), 1034-1047. doi:10.1016/j.cmet.2016.05.007

Chazotte, B. (2011). Labeling lysosomes in live cells with LysoTracker. *Cold Spring Harb Protoc, 2011*(2), pdb prot5571. doi:10.1101/pdb.prot5571

Chen, X., Ba, Y., Ma, L., Cai, X., Yin, Y., Wang, K., . . . Zhang, C. Y. (2008). Characterization of microRNAs in serum: a novel class of biomarkers for diagnosis of cancer and other diseases. *Cell Res, 18*(10), 997-1006. doi:10.1038/cr.2008.282

Cheng, M., Yang, J., Zhao, X., Zhang, E., Zeng, Q., Yu, Y., . . . Qin, G. (2019). Circulating myocardial microRNAs from infarcted hearts are carried in exosomes and mobilise bone marrow progenitor cells. *Nat Commun, 10*(1), 959. doi:10.1038/s41467-019-08895-7

Chung, C. Y., Shin, H. R., Berdan, C. A., Ford, B., Ward, C. C., Olzmann, J. A., . . . Nomura, D. K. (2019). Covalent targeting of the vacuolar H(+)-ATPase activates autophagy via mTORC1 inhibition. *Nat Chem Biol, 15*(8), 776-785. doi:10.1038/s41589-019-0308-4

Cruz-Jentoft, A. J., Baeyens, J. P., Bauer, J. M., Boirie, Y., Cederholm, T., Landi, F., . . . European Working Group on Sarcopenia in Older, P. (2010). Sarcopenia: European consensus on definition and diagnosis: Report of the European Working Group on Sarcopenia in Older People. *Age Ageing, 39*(4), 412-423. doi:10.1093/ageing/afq034

D'Souza, R. F., Woodhead, J. S. T., Zeng, N., Blenkiron, C., Merry, T. L., Cameron-Smith, D., & Mitchell, C. J. (2018). Circulatory exosomal miRNA following intense exercise is unrelated to muscle and plasma miRNA abundances. *Am J Physiol Endocrinol Metab, 315*(4), E723-E733. doi:10.1152/ajpendo.00138.2018

Demontis, F., Piccirillo, R., Goldberg, A. L., & Perrimon, N. (2013). Mechanisms of skeletal muscle aging: insights from Drosophila and mammalian models. *Dis Model Mech, 6*(6), 1339-1352. doi:10.1242/dmm.012559

Distefano, G., & Goodpaster, B. H. (2018). Effects of Exercise and Aging on Skeletal Muscle. *Cold Spring Harb Perspect Med, 8*(3). doi:10.1101/cshperspect.a029785

Dowling, J. J., Moore, S. A., Kalimo, H., & Minassian, B. A. (2015). X-linked myopathy with excessive autophagy: a failure of self-eating. *Acta Neuropathol, 129*(3), 383-390. doi:10.1007/s00401-015-1393-4

884   Ejlerskov, P., Rubinsztein, D. C., & Pocock, R. (2020). IFNB/interferon-beta regulates
885   autophagy via a MIR1-TBC1D15-RAB7 pathway. *Autophagy, 16*(4), 767-769.
886   doi:10.1080/15548627.2020.1718384
887   Gerisch, B., Rottiers, V., Li, D., Motola, D. L., Cummins, C. L., Lehrach, H., . . . Antebi, A.
888   (2007). A bile acid-like steroid modulates Caenorhabditis elegans lifespan through
889   nuclear receptor signaling. *Proc Natl Acad Sci U S A, 104*(12), 5014-5019.
890   doi:10.1073/pnas.0700847104
891   Grosswendt, S., Filipchyk, A., Manzano, M., Klironomos, F., Schilling, M., Herzog, M., . . .
892   Rajewsky, N. (2014). Unambiguous identification of miRNA:target site interactions by
893   different types of ligation reactions. *Mol Cell, 54*(6), 1042-1054.
894   doi:10.1016/j.molcel.2014.03.049
895   Gu, S., & Kay, M. A. (2010). How do miRNAs mediate translational repression? *Silence, 1*(1),
896   11. doi:10.1186/1758-907X-1-11
897   Guo, Z., Maki, M., Ding, R., Yang, Y., Zhang, B., & Xiong, L. (2014). Genome-wide survey of
898   tissue-specific microRNA and transcription factor regulatory networks in 12 tissues.
899   *Sci Rep, 4*, 5150. doi:10.1038/srep05150
900   Hermann, G. J., Schroeder, L. K., Hieb, C. A., Kershner, A. M., Rabbitts, B. M., Fonarev,
901   P., . . . Priess, J. R. (2005). Genetic analysis of lysosomal trafficking in
902   Caenorhabditis elegans. *Mol Biol Cell, 16*(7), 3273-3288. doi:10.1091/mbc.e05-01-
903   0060
904   Herndon, L. A., Schmeissner, P. J., Dudaronek, J. M., Brown, P. A., Listner, K. M., Sakano,
905   Y., . . . Driscoll, M. (2002). Stochastic and genetic factors influence tissue-specific
906   decline in ageing C. elegans. *Nature, 419*(6909), 808-814. doi:10.1038/nature01135
907   Hua, L., Zhu, G., & Wei, J. (2018). MicroRNA-1 overexpression increases chemosensitivity of
908   non-small cell lung cancer cells by inhibiting autophagy related 3-mediated
909   autophagy. *Cell Biol Int, 42*(9), 1240-1249. doi:10.1002/cbin.10995
910   Ibanez-Ventoso, C., Herrera, C., Chen, E., Motto, D., & Driscoll, M. (2016). Automated
911   Analysis of C. elegans Swim Behavior Using CeleST Software. *J Vis Exp*(118).
912   doi:10.3791/54359
913   Ivey, K. N., Muth, A., Arnold, J., King, F. W., Yeh, R. F., Fish, J. E., . . . Srivastava, D. (2008).
914   MicroRNA regulation of cell lineages in mouse and human embryonic stem cells. *Cell*
915   *Stem Cell, 2*(3), 219-229. doi:10.1016/j.stem.2008.01.016
916   Jan, C. H., Friedman, R. C., Ruby, J. G., & Bartel, D. P. (2011). Formation, regulation and
917   evolution of Caenorhabditis elegans 3'UTRs. *Nature, 469*(7328), 97-101.
918   doi:10.1038/nature09616
919   Kamath, R. S., & Ahringer, J. (2003). Genome-wide RNAi screening in Caenorhabditis
920   elegans. *Methods, 30*(4), 313-321. doi:10.1016/s1046-2023(03)00050-1
921   Lall, S., Grun, D., Krek, A., Chen, K., Wang, Y. L., Dewey, C. N., . . . Rajewsky, N. (2006). A
922   genome-wide map of conserved microRNA targets in C. elegans. *Curr Biol, 16*(5),
923   460-471. doi:10.1016/j.cub.2006.01.050
924   Liegeois, S., Benedetto, A., Garnier, J. M., Schwab, Y., & Labouesse, M. (2006). The V0-
925   ATPase mediates apical secretion of exosomes containing Hedgehog-related
926   proteins in Caenorhabditis elegans. *J Cell Biol, 173*(6), 949-961.
927   doi:10.1083/jcb.200511072
928   Lin, X. X., Sen, I., Janssens, G. E., Zhou, X., Fonslow, B. R., Edgar, D., . . . Riedel, C. G.
929   (2018). DAF-16/FOXO and HLH-30/TFEB function as combinatorial transcription
930   factors to promote stress resistance and longevity. *Nat Commun, 9*(1), 4400.
931   doi:10.1038/s41467-018-06624-0

932   Liu, N., Bezprozvannaya, S., Shelton, J. M., Frisard, M. I., Hulver, M. W., McMillan, R. P., . . .
933   Olson, E. N. (2011). Mice lacking microRNA 133a develop dynamin 2-dependent
934   centronuclear myopathy. *J Clin Invest, 121*(8), 3258-3268. doi:10.1172/JCI46267
935   Martinez, N. J., Ow, M. C., Reece-Hoyes, J. S., Barrasa, M. I., Ambros, V. R., & Walhout, A.
936   J. (2008). Genome-scale spatiotemporal analysis of Caenorhabditis elegans
937   microRNA promoter activity. *Genome Res, 18*(12), 2005-2015.
938   doi:10.1101/gr.083055.108
939   Martinez, V. G., Javadi, C. S., Ngo, E., Ngo, L., Lagow, R. D., & Zhang, B. (2007). Age-
940   related changes in climbing behavior and neural circuit physiology in Drosophila. *Dev
941   Neurobiol, 67*(6), 778-791. doi:10.1002/dneu.20388
942   Miller, M. S., Lekkas, P., Braddock, J. M., Farman, G. P., Ballif, B. A., Irving, T. C., . . .
943   Vigoreaux, J. O. (2008). Aging enhances indirect flight muscle fiber performance yet
944   decreases flight ability in Drosophila. *Biophys J, 95*(5), 2391-2401.
945   doi:10.1529/biophysj.108.130005
946   Miska, E. A., Alvarez-Saavedra, E., Abbott, A. L., Lau, N. C., Hellman, A. B., McGonagle, S.
947   M., . . . Horvitz, H. R. (2007). Most Caenorhabditis elegans microRNAs are
948   individually not essential for development or viability. *PLoS Genet, 3*(12), e215.
949   doi:10.1371/journal.pgen.0030215
950   Mitchelson, K. R., & Qin, W. Y. (2015). Roles of the canonical myomiRs miR-1, -133 and -
951   206 in cell development and disease. *World J Biol Chem, 6*(3), 162-208.
952   doi:10.4331/wjbc.v6.i3.162
953   Morley, J. F., Brignull, H. R., Weyers, J. J., & Morimoto, R. I. (2002). The threshold for
954   polyglutamine-expansion protein aggregation and cellular toxicity is dynamic and
955   influenced by aging in Caenorhabditis elegans. *Proc Natl Acad Sci U S A, 99*(16),
956   10417-10422. doi:10.1073/pnas.152161099
957   Nair, K. S. (2005). Aging muscle. *Am J Clin Nutr, 81*(5), 953-963. doi:10.1093/ajcn/81.5.953
958   Nehammer, C., Ejlerskov, P., Gopal, S., Handley, A., Ng, L., Moreira, P., . . . Pocock, R.
959   (2019). Interferon-beta-induced miR-1 alleviates toxic protein accumulation by
960   controlling autophagy. *Elife, 8*. doi:10.7554/eLife.49930
961   O'Rourke, E. J., & Ruvkun, G. (2013). MXL-3 and HLH-30 transcriptionally link lipolysis and
962   autophagy to nutrient availability. *Nat Cell Biol, 15*(6), 668-676. doi:10.1038/ncb2741
963   Panwar, B., Omenn, G. S., & Guan, Y. (2017). miRmine: a database of human miRNA
964   expression profiles. *Bioinformatics, 33*(10), 1554-1560.
965   doi:10.1093/bioinformatics/btx019
966   Perez-Riverol, Y., Csordas, A., Bai, J., Bernal-Llinares, M., Hewapathirana, S., Kundu, D.
967   J., . . . Vizcaino, J. A. (2019). The PRIDE database and related tools and resources in
968   2019: improving support for quantification data. *Nucleic Acids Res, 47*(D1), D442-
969   D450. doi:10.1093/nar/gky1106
970   Pollock, R. D., O'Brien, K. A., Daniels, L. J., Nielsen, K. B., Rowlerson, A., Duggal, N. A., . . .
971   Harridge, S. D. R. (2018). Properties of the vastus lateralis muscle in relation to age
972   and physiological function in master cyclists aged 55-79 years. *Aging Cell, 17*(2).
973   doi:10.1111/acel.12735
974   Restif, C., Ibanez-Ventoso, C., Vora, M. M., Guo, S., Metaxas, D., & Driscoll, M. (2014).
975   CeleST: computer vision software for quantitative analysis of C. elegans swim
976   behavior reveals novel features of locomotion. *PLoS Comput Biol, 10*(7), e1003702.
977   doi:10.1371/journal.pcbi.1003702
978   Rual, J. F., Ceron, J., Koreth, J., Hao, T., Nicot, A. S., Hirozane-Kishikawa, T., . . . Vidal, M.
979   (2004). Toward improving Caenorhabditis elegans phenome mapping with an

ORFeome-based RNAi library. *Genome Res, 14*(10B), 2162-2168. doi:10.1101/gr.2505604

Sardiello, M., Palmieri, M., di Ronza, A., Medina, D. L., Valenza, M., Gennarino, V. A., . . . Ballabio, A. (2009). A gene network regulating lysosomal biogenesis and function. *Science, 325*(5939), 473-477. doi:10.1126/science.1174447

Settembre, C., Di Malta, C., Polito, V. A., Garcia Arencibia, M., Vetrini, F., Erdin, S., . . . Ballabio, A. (2011). TFEB links autophagy to lysosomal biogenesis. *Science, 332*(6036), 1429-1433. doi:10.1126/science.1204592

Settembre, C., Fraldi, A., Medina, D. L., & Ballabio, A. (2013). Signals from the lysosome: a control centre for cellular clearance and energy metabolism. *Nat Rev Mol Cell Biol, 14*(5), 283-296. doi:10.1038/nrm3565

Simon, D. J., Madison, J. M., Conery, A. L., Thompson-Peer, K. L., Soskis, M., Ruvkun, G. B., . . . Kim, J. K. (2008). The microRNA miR-1 regulates a MEF-2-dependent retrograde signal at neuromuscular junctions. *Cell, 133*(5), 903-915. doi:10.1016/j.cell.2008.04.035

Snel, B., Lehmann, G., Bork, P., & Huynen, M. A. (2000). STRING: a web-server to retrieve and display the repeatedly occurring neighbourhood of a gene. *Nucleic Acids Res, 28*(18), 3442-3444. doi:10.1093/nar/28.18.3442

Stark, A., Brennecke, J., Bushati, N., Russell, R. B., & Cohen, S. M. (2005). Animal MicroRNAs confer robustness to gene expression and have a significant impact on 3'UTR evolution. *Cell, 123*(6), 1133-1146. doi:10.1016/j.cell.2005.11.023

Tharyan, R. G., Annibal, A., Schiffer, I., Laboy, R., Atanassov, I., Weber, A. L., . . . Antebi, A. (2020). NFYB-1 regulates mitochondrial function and longevity via lysosomal prosaposin. *Nat Metab, 2*(5), 387-396. doi:10.1038/s42255-020-0200-2

Wang, S., Wong, L. Y., Neumann, D., Liu, Y., Sun, A., Antoons, G., . . . Luiken, J. (2020). Augmenting Vacuolar H(+)-ATPase Function Prevents Cardiomyocytes from Lipid-Overload Induced Dysfunction. *Int J Mol Sci, 21*(4). doi:10.3390/ijms21041520

Weber, J. A., Baxter, D. H., Zhang, S., Huang, D. Y., Huang, K. H., Lee, M. J., . . . Wang, K. (2010). The microRNA spectrum in 12 body fluids. *Clin Chem, 56*(11), 1733-1741. doi:10.1373/clinchem.2010.147405

Wust, S., Drose, S., Heidler, J., Wittig, I., Klockner, I., Franko, A., . . . Braun, T. (2018). Metabolic Maturation during Muscle Stem Cell Differentiation Is Achieved by miR-1/133a-Mediated Inhibition of the Dlk1-Dio3 Mega Gene Cluster. *Cell Metab, 27*(5), 1026-1039 e1026. doi:10.1016/j.cmet.2018.02.022

Xu, J., Cao, D., Zhang, D., Zhang, Y., & Yue, Y. (2020). MicroRNA-1 facilitates hypoxia-induced injury by targeting NOTCH3. *J Cell Biochem, 121*(11), 4458-4469. doi:10.1002/jcb.29663

Zhang, C. S., Jiang, B., Li, M., Zhu, M., Peng, Y., Zhang, Y. L., . . . Lin, S. C. (2014). The lysosomal v-ATPase-Ragulator complex is a common activator for AMPK and mTORC1, acting as a switch between catabolism and anabolism. *Cell Metab, 20*(3), 526-540. doi:10.1016/j.cmet.2014.06.014

Zhao, Y., Ransom, J. F., Li, A., Vedantham, V., von Drehle, M., Muth, A. N., . . . Srivastava, D. (2007). Dysregulation of cardiogenesis, cardiac conduction, and cell cycle in mice lacking miRNA-1-2. *Cell, 129*(2), 303-317. doi:10.1016/j.cell.2007.03.030
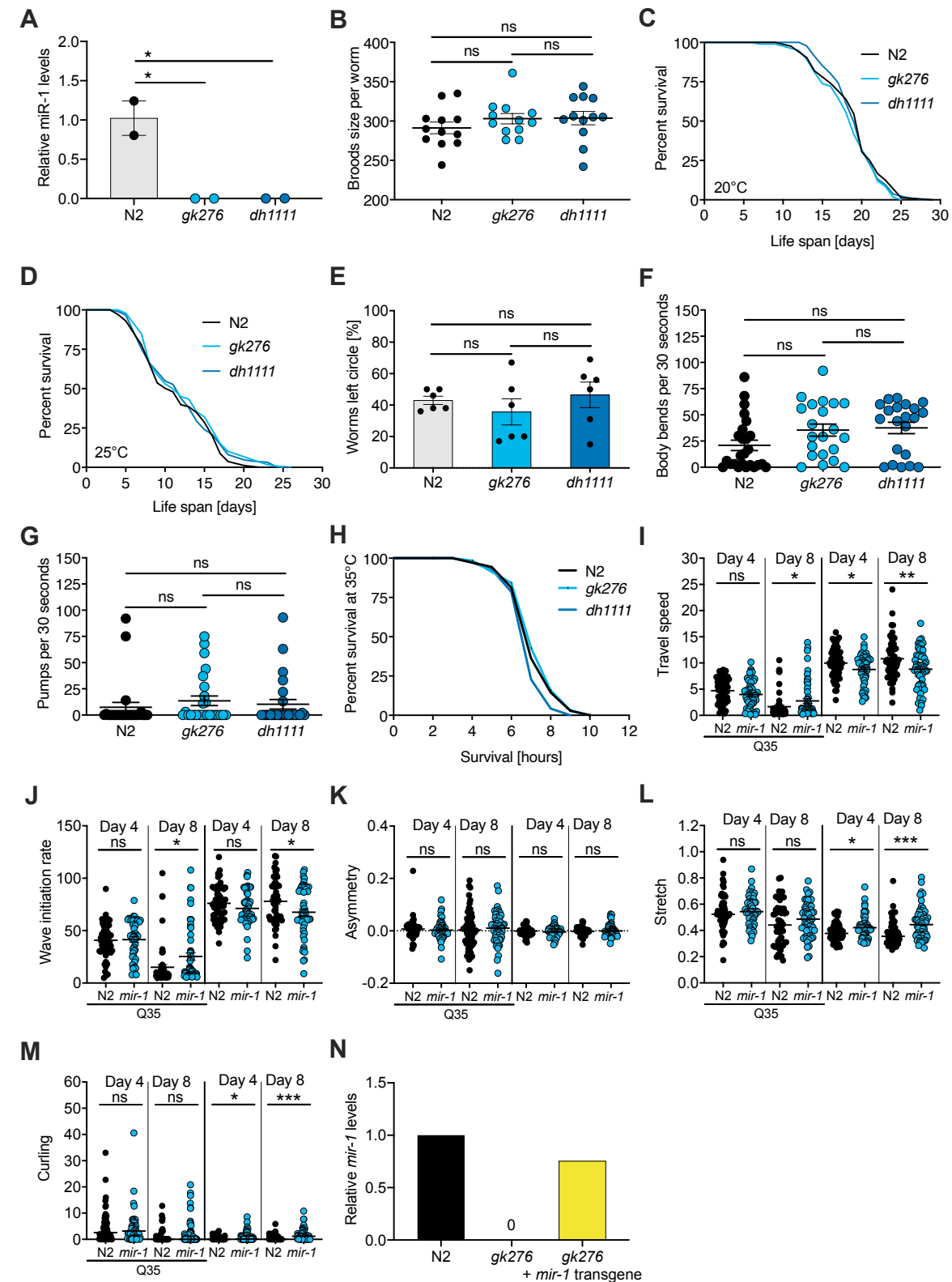
Acknowledgements

Contributions

IS, BG, KK, RL, JH, MSD, YS, AA designed and performed experiments

IS, BG, SV, OS, AA wrote the paper

34

Supplementary data

Supplementary Figure 1. (linked to Figure 1)

(A) TaqMan qPCR measuring mature *mir-1* levels show that the deletion alleles do not express *mir-1* and are null, N=2 BR. mean ± SEM, one way ANOVA, *, p<0.05.

1051   **(B)** Brood size of *mir-1(gk276)* and *mir-1(dh1111)* compared to wild-type (N2). Each dot represents the

1052   brood size of one worm, mean ± SEM, one way ANOVA, ns, not significant.

1053   **(C)** and **(D)** Lifespan experiments performed at 20°C and 25°C for two *mir-1* deletion alleles compared

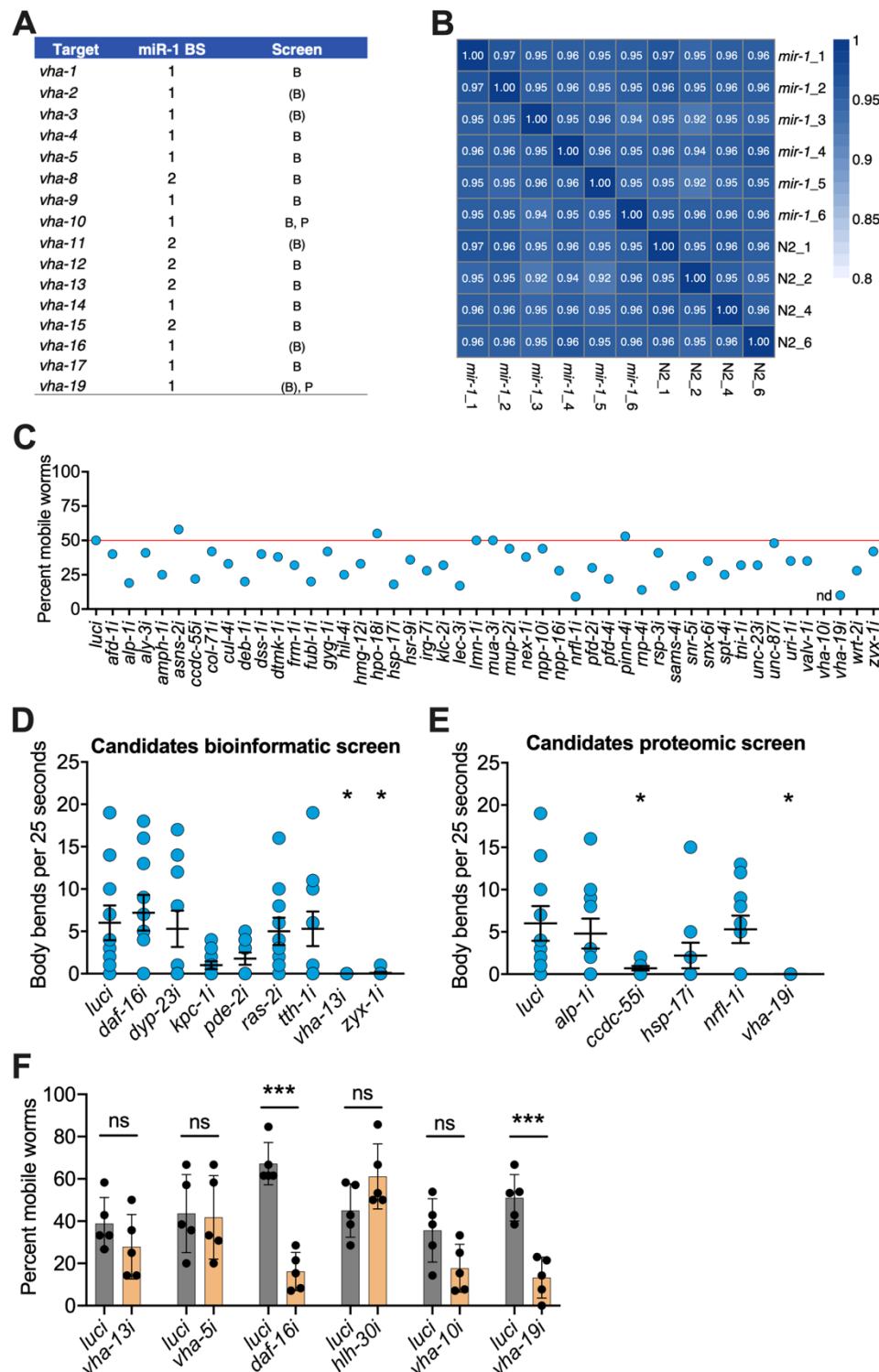1054   to wild-type. N=3. Not significant (Supplemental Table 1).

1055   **(E)** and **(F)** Motility of wild-type and *mir-1(gk276)* mutant animals on day 14 of adulthood, measured by

1056   circle test (E) and thrashing in liquid (F). One representative experiment of each N=3 is shown. Mean ±

1057   SEM, one way ANOVA, ns, not significant.

1058   **(G)** Pharyngeal pumping rate measured on day 14 in two *mir-1* alleles compared to wild-type. N=3, one

1059   representative experiment is shown. Mean ± SEM, one way ANOVA, ns, not significant.

1060   **(H)** Heat stress survival at 35°C of day 1 *mir-1(gk276)* and *mir-1 (dh1111)* mutants compared to wild-

1061   type. One representative experiment is shown, N=3, t-test: N2 *vs. gk276*: p=0.20. N2 *vs. dh1111*:

1062   p=0.17.

1063   **(I)** to **(M)** CeleST locomotion behaviour analyses of wild-type and *mir-1(gk276)* mutant animals with or

1064   without *unc-54p::Q35::YFP*, at day 4 and day 8 of adulthood. Each dot represents one animal. **(I)** travel

1065   speed **(J)** wave initiation rate **(K)** asymmetry **(L)** stretch, and **(M)** curling. t-test, *, p<0.05, **, p<0.01,

1066   ***, p<0.001, ns, not significant.

1067   **(N)** Bar graph showing the expression level of mature miR-1 microRNA in the indicated genotypes. N=1

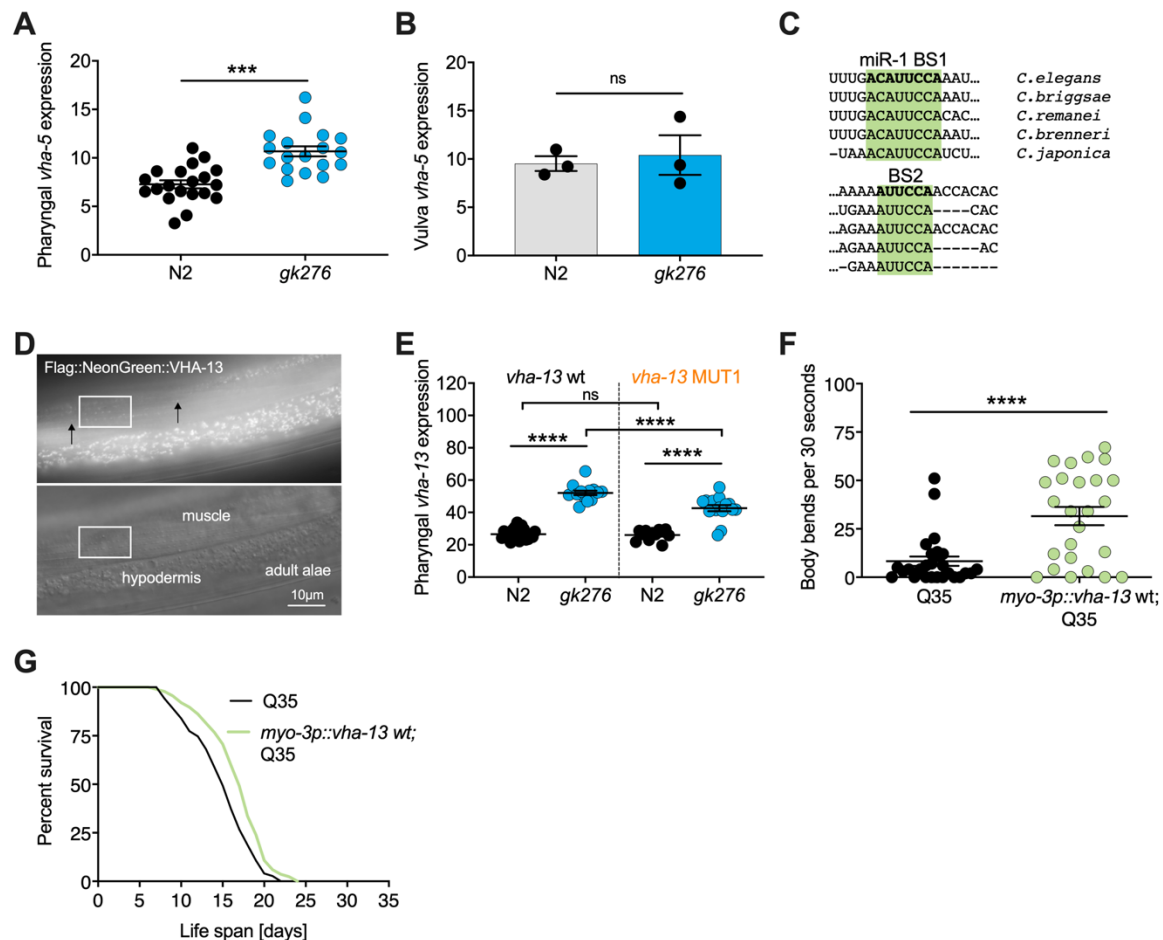1068   biological replicate, 4 technical replicates.

1069

1070

1071

1072

Supplementary Figure 2. (linked to Figure 2)

(A) v-ATPase subunits containing one or two predicted miR-1 binding sides (BS) in their 3'UTR. v-ATPase genes identified in the bioinformatic screen by all three databases are labelled „B", by 2 databases are labelled „(B)" and by the proteomic screen are labelled „P".

(B) Correlation plot of the biological replicates from proteomics showing the similarity of WT (N2) and *mir-1* genotypes.

1079   **(C)** RNAi screen for genes required for *mir-1(gk276)*;Q35 motility in the circle test, using upregulated

1080   genes from the proteomic analysis (Supplemental Tables 5 and 6). Each dot represents the percentage

1081   of worms that left the circle. Red line, percent luciferase controls that left the circle. Nd, not determined.

1082   Validation of selected candidates identified from bioinformatic **(D)** and **(E)** proteomic screens by

1083   thrashing assay on day 8 of adulthood. *mir-1(gk276)*;Q35 worms were grown on the corresponding

1084   RNAi from L4 onwards. Each dot represents one animal, 15 worms per RNAi. Mean ± SEM, one way

1085   ANOVA, only significant values are labelled: *, $p < 0.05$.

1086   **(F)** Motility of worms in circle test of indicated RNAi on N2;Q35 worms. Motility was measured on day 5

1087   of adulthood, each dot represents the percentage of worms that left the circle. Mean ± SEM of one

1088   representative experiment, N=3, one way ANOVA, ***, $p < 0.001$, ns, not significant.

1089

1090

38

Supplementary Figure 3. (linked to Figure 3)

(A) Quantification of pharyngeal fluorescent intensity of endogenous *3xFlag::mNeon Green::vha-5* expression in indicated genotypes in late L4s maintained at 25°C. One representative experiment of N=3, mean ± SEM, t-test, ***, p<0.001.

(B) Quantification of fluorescent intensity of *3xFlag::mNeonGreen::vha-5* expression in the vulva of indicated genotypes. Mean ± SEM of N=3, t-test, ns, not significant.

(C) Schematic showing the conservation of miR-1 binding sites (BS) in the *vha-13* 3'UTR of different nematode species.

(D) Images showing expression of endogenously tagged *3xFlag::mNeonGreen::vha-13* in muscle dense body and hypodermis. Arrows indicate individual dense bodies. Rectangle highlights muscle section shown in Figure 3B.
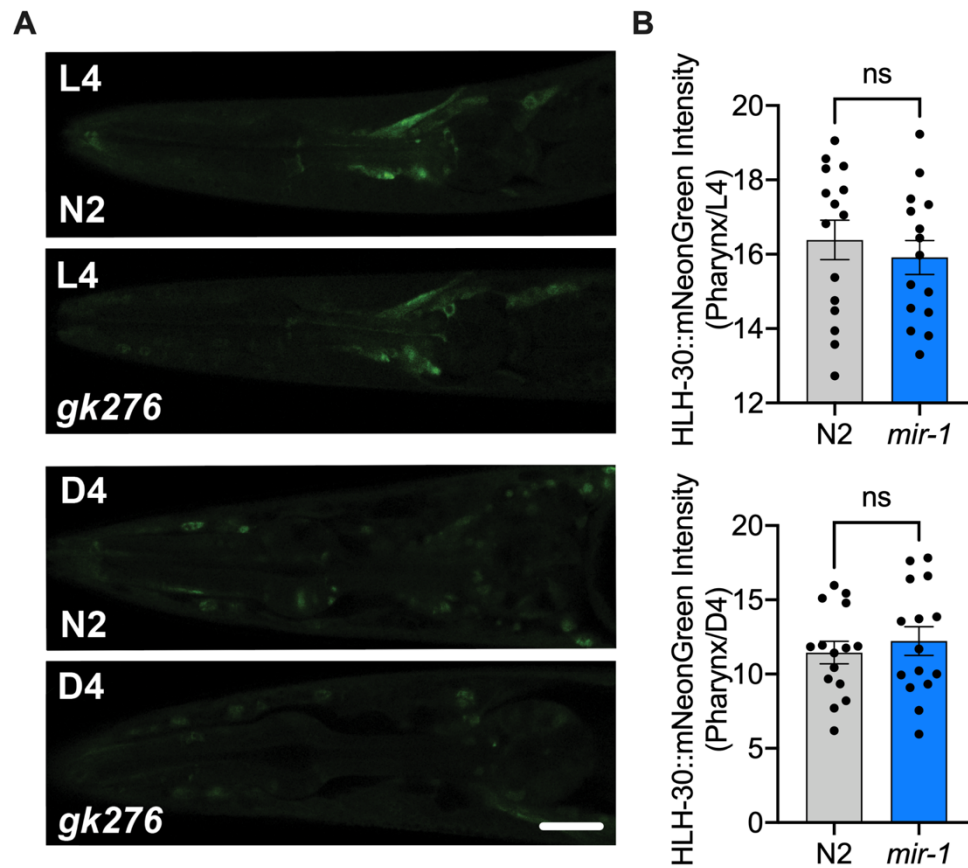
(E) Quantification of fluorescence intensity in the isthmus of L4 larvae with endogenously tagged *3xFlag::mNeonGreen::vha-13* with *vha-13* MUT1 3' UTR in relation to *vha-13* wt 3'UTR, in N2 and *mir-1(gk276)* mutant backgrounds using confocal microscopy. Mean ± SEM of one representative experiment. N=2, one way ANOVA, ****, p<0.00001, ns not significant.

(F) Thrashing assay of *unc-54p::Q35::YFP* (Q35) worms expressing *vha-13* in body wall muscle (*myo3p::vha-13* wt;Q35) or non-transgenic Q35 animals. 25 worms per genotype, mean ± SEM of one representative experiment, N=4, t-test, ****, p<0.0001.

39

1110   **(G)** Life span of Q35 worms overexpressing *vha-13* in the body wall muscle (*myo3p*::*vha-13* wt;Q35)

1111   and Q35 non-transgenic segregants of the same strain. One experiment of N=4. Life span effects of two

1112   experiments were significant (Supplemental Table 1). t-test: 0.0017.

1113

1114

1115

A

B

1116

1117 **Supplementary Figure 4. (linked to Figure 4)**

1118 **(A)** Fluorescent image comparing HLH-30::mNeonGreen intensity in the pharynx of the *mir-1(gk276)*

1119 and WT (N2) backgrounds in L4s (top) or day 4 adults (D4, bottom). Scale bar 20 µm **(B)** Quantitation

1120 of nuclear localization in **(A)**, dots represent individual animals. N=2 biological replicates for L4 and N=1

1121 for day 4 adults, t-test, ns: not significant.

1122

1123

1124   Supplemental Table 1: Lifespan and heat stress data.

1125   Supplemental Table 2: Q35 aggregate and behavior data.

1126   Supplemental Table 3: CeleSt data.

1127   Supplemental Table 4: Bioinformatic screen data.

1128   Supplemental Table 5: RNAi motility screen.

1129   Supplemental Table 6: Proteomic analysis of differentially regulated proteins in *mir-1*

1130   *vs.* wildtype.

1131   Supplemental Table 7: Microscopy data.

1132   Supplemental Table 8: Primers.